



Publication Year	2018
Acceptance in OA	2021-04-15T15:33:39Z
Title	Improved estimation of Mars ionosphere total electron content
Authors	CARTACCI, MARCO, Sánchez-Cano, B., OROSEI, ROBERTO, NOSCHESE, RAFFAELLA, CICCHETTI, ANDREA, Witasse, O., Cantini, F., Rossi, A. P.
Publisher's version (DOI)	10.1016/j.icarus.2017.07.033
Handle	http://hdl.handle.net/20.500.12386/30761
Journal	ICARUS
Volume	299

1 Improved estimation of Mars ionosphere total electron content

2

3

4

5 M. Cartacci^{1*}, B. Sánchez-Cano², R. Orosei⁴, R. Noschese¹, A. Cicchetti¹, O. Witasse³, F. Cantini⁵,
6 A. P. Rossi⁶

7

8

9

10

11 ¹Istituto di Astrofisica e Planetologia Spaziali (IAPS), Istituto Nazionale di Astrofisica (INAF),
12 Rome, Italy.

13 ²Radio and Space Plasma Physics Group, Department of Physics and Astronomy, University of
14 Leicester, University Road, Leicester LE1 7RH, United Kingdom,

15 ³European Space Agency, ESTEC – Scientific Support Office, Keplerlaan 1, Noordwijk 2200 AG,
16 The Netherlands

17 ⁴ Istituto di Radioastronomia (IRA), Istituto Nazionale di Astrofisica (INAF), Bologna, Italy

18 ⁵ Ecole Polytechnique Federale de Lausanne, Space Engineering Center, EPFL ESC, Station 13,
19 1015 Lausanne, Switzerland

20 ⁶ Department of Physics and Earth Sciences, Jacobs University Bremen, Campus Ring 1, 28759
21 Bremen, Germany

22 *Corresponding author.

23 E-mail address: marco.cartacci@iaps.inaf.it (Marco Cartacci, Rome, Italy)

24 bscmdr1@leicester.ac.uk (Beatriz Sánchez-Cano, Leicester, United Kingdom)

25 roberto.oroisei@inaf.it (Roberto Orosei, Rome, Italy)

26 raffaella.noschese@iaps.inaf.it (Raffaella Noschese, Rome, Italy)

27 andrea.cicchetti@iaps.inaf.it (Andrea Cicchetti, Rome, Italy)
28 owitasse@cosmos.esa.int (Olivier Witasse, Noordwijk, The Netherlands)
29 federico.cantini@epfl.ch (Federico Cantini, Lausanne, Switzerland)
30 an.rossi@jacobs-university.de (Angelo Pio Rossi, Bremen, Germany)

31

32

33

34

35

36

37

38

39

40

41

42

43

44

45

46

47

48

49

50

51

52

53 **ABSTRACT**

54 We describe an improved method to estimate the Total Electron Content (TEC) of the Mars
55 ionosphere from the echoes recorded by the Mars Advanced Radar for Subsurface and Ionosphere
56 Sounding (MARSIS) (Picardi et al. 2005, Orosei et al. 2015) onboard Mars Express in its
57 subsurface sounding mode. In particular, we demonstrate that this method solves the issue of the
58 former algorithm described at (Cartacci et al., 2013), which produced an overestimation of TEC
59 estimates on the day side.

60 The MARSIS signal is affected by a phase distortion introduced by the Mars ionosphere that
61 produces a variation of the signal shape and a delay in its travel time. The new TEC estimation is
62 achieved correlating the parameters obtained through the correction of the aforementioned effects.

63 In detail, the knowledge of the quadratic term of the phase distortion estimated by the Contrast
64 Method (Cartacci et al., 2013), together with the linear term (i.e. the extra time delay), estimated
65 through a radar signal simulator, allows to develop a new algorithm particularly well suited to
66 estimate the TEC for solar zenith angles (SZA) lower than 95° . The new algorithm for the dayside
67 has been validated with independent data from MARSIS in its Active Ionospheric Sounding (AIS)
68 operational mode, with comparisons with other previous algorithms based on MARSIS subsurface
69 data, with modeling and with modeling ionospheric distortion TEC reconstruction.

70

71

72

73 **1. Introduction**

74 The Mars ionosphere is created by the ionization of the neutral atmosphere and its electron density
75 is the result of a dynamic balance between the production and loss processes of free charged
76 species.

77 The density of the free electrons N_e vary substantially with location, solar illumination, solar
78 activity and season, due to complex interactions between solar photon fluxes and solar wind with
79 the neutral gas. The Mars case is even more complicated due the absence of an appreciable global
80 magnetic field and the presence of magnetic crustal anomalies, that produce a direct interaction
81 between the ionosphere and the solar wind.

82

83 The use of a low-frequency radar sounder to analyse the surface and subsurface of Mars, such as
84 the Mars Advanced Radar for Subsurface and Ionosphere Sounding (MARSIS) on board Mars
85 Express (Picardi et al., 2005), must take into account the dispersion caused by the ionosphere on
86 the propagating signal, which depends on the operative frequencies adopted.

87 In this paper, we report about improved processing procedures, implemented in order to remove the
88 effects of the ionosphere from the radar signal, because what was a problem for the sounding of the
89 subsurface becomes a useful source of information in the study of the ionosphere. The outcome of
90 this processing is a data set of high-accuracy values of the Total Electron Content (TEC) of the full
91 atmosphere, covering about 10 years of scientific operations of the MARSIS radar.

92

93 In the following, section 2 contains a brief description of the main effects of the Martian ionosphere
94 on radar propagation; section 3 describes the MARSIS instrument; section 4 describes the methods
95 developed to compensate the ionosphere effects, the description of the new algorithm for the TEC
96 estimation and the results obtained, while section 5 contains a discussion of the results and a brief
97 summary and a discussion of possible future developments.

98 2. The effects of the Mars ionosphere on MARSIS signal propagation

99 The presence of the Martian ionosphere produces a variation of the refraction index with respect to
100 vacuum. As a consequence, for an electromagnetic wave of frequency f , the propagation in the
101 ionosphere is characterized by the following refraction index (Safaeinili et al. 2007):

$$102 \quad n(z) = \sqrt{1 - \frac{f_p^2(z)}{f^2}} \quad (1)$$

103
104 where f_p is the plasma frequency and z is the altitude above ground. The plasma frequency, in Hz,
105 can be written as

$$106 \quad f_p(z) = 8.98 \sqrt{N_e(z)}, \quad (2)$$

107 where N_e is the electron density in m^{-3} .

108 According to Eq. (1) all frequencies lower than f_p will be reflected, while those higher will be
109 delayed. Moreover, since the radio wave propagation speed varies according to the refraction index
110 and the frequency in the bandwidth, the chirp will be affected by phase dispersion (Budden, 1985).
111 Therefore, in the presence of an ionosphere, the signals will be attenuated, delayed and defocused
112 with different levels of severity depending on the electron density values encountered along the path
113 (Cartacci et al., 2013). All these effects, if not compensated, can drastically reduce the quality of the
114 data. In particular, the defocusing distorts the waveform shape, worsening the signal to noise ratio
115 and the range resolution (see fig. 1, Cartacci et al., 2013).

116 In order to remove, or at least reduce, the distortion, a dedicated algorithm was developed, called
117 the Contrast Method (Picardi et al. 2000, Cartacci et al., 2013) and was implemented in both on-
118 board and on-ground processing. The Contrast Method (hereafter CM) does not compensate the
119 group delay of the radar pulse. The correct arrival time of the echo can be estimated from the
120 spacecraft altitude above the surface, or by using simulations of surface scattering of the radar pulse
121 (see e.g. Nouvel et al., 2004; Russo et al., 2008).

122 3. The MARSIS instrument

123 The Mars Advanced Radar for Subsurface and Ionosphere Sounding (MARSIS) (Picardi et al.
124 2005), carried by ESA's Mars Express spacecraft, is a nadir-looking pulse-limited radar sounder,
125 which uses synthetic aperture (SAR) techniques to achieve a higher signal-to-noise ratio and along-
126 track resolution. MARSIS was developed by the University of Rome "La Sapienza", Italy, in
127 partnership with NASA's Jet Propulsion Laboratory in Pasadena, California. The main task of the
128 MARSIS experiment is to map the distribution of water, both liquid and solid, on Mars, with the
129 secondary objective of characterizing the structure of the Martian ionosphere. In order to achieve
130 these goals, MARSIS has two operation modes: the SS (Sub-Surface) Mode and the AIS (Active
131 Ionosphere Sounding) Mode.

132 When sets in AIS Mode, MARSIS works as a swept frequency sounder, transmitting 160 spaced
133 frequencies from 100 kHz to 5.5 MHz (Morgan et al. 2008). In this way, the radar is able to
134 characterized the upper profile of the ionosphere estimating the topside electron density N_e . These
135 in-situ measurements, must be considered as a reference for any study related to the Mars
136 ionosphere.

137 In its Sub-Surface (SS) mode, MARSIS transmits "chirps", i.e. wave packets of duration $T = 250$
138 μsec which are linearly modulated in frequency over a bandwidth $B = 1$ MHz, centred at 1.8 MHz,
139 3 MHz, 4 MHz or 5 MHz, alternating the transmission at two different frequencies, from a 40-m
140 dipole antenna with a Pulse Repetition Frequency (PRF) of 127 Hz. MARSIS frequencies are
141 optimized for deep penetration of the surface of Mars but are vulnerable to ionospheric effects; for
142 this reason, the two frequencies are chosen according to the Solar Zenith Angle (SZA) at the time of
143 observation, in order to have the transmitted bandwidth always higher than the local plasma
144 frequency, and therefore, be able to penetrate the full atmosphere with the smallest possible
145 degradation. As the electron density is known to be lower in the night side (Gurnett, D. A., et al.
146 2008), this constraint implies that the MARSIS subsurface sounder is best utilized for values of

147 SZA higher than 90°. For this reason, normally during the night side (SZA ≥ 90°) the carrier
 148 frequencies used are 4 MHz and 3 MHz, while during the day side (SZA < 90°) the carrier
 149 frequencies used are 5 MHz and 4 MHz. The lowest frequency of 1.8 MHz is rarely used because it
 150 can only work properly during the deep night side (SZA > 115°) (see fig. 5, Cartacci et al. 2013) and
 151 it is more vulnerable to local variation of the ionosphere than higher frequencies.

152 Along an orbit, the MARSIS radar performs a large number of synthetic apertures (frames). Each
 153 frame consists of about 200 radar pulses (this value depends on different parameters such as signal
 154 frequency, altitude, tangential velocity etc.), transmitted in a segment of orbit at least 5,5 km long
 155 (minimum value for a single synthetic aperture). Typically, between two frames the SZA variation
 156 it is around 0.05°/0.06°, so we assumed the ionosphere as stationary within a single synthetic
 157 aperture.

158 The on-board processing consists of two steps: the azimuth compression, where the echoes received
 159 for each transmitted pulse are integrated together (unfocused SAR) and the range compression,
 160 which is the product, in the frequency domain, between the integrated signal and a matched filter
 161 (an ideal “chirp” used as reference function).

162 The next step consists in the tracking phase, where the signal position inside the receiving window
 163 is checked. It is worth noting that the signal travel time can vary considerably according to the Mars
 164 surface topography and the presence or not of an extra delay time due to the ionosphere.

165 For this reason, MARSIS is equipped with a tracking loop working with an Offset Center Of
 166 Gravity (O.C.O.G.) algorithm (Wingham et al. 1986).

$$167 \quad OCOG = \frac{\sum_{i=ini_ind}^{last_ind} i \cdot P_D(i)}{\sum_{i=ini_ind}^{last_ind} P_D(i)} - \frac{\left[\sum_{i=ini_ind}^{last_ind} P_D(i) \right]^2}{2 \cdot \sum_{i=ini_ind}^{last_ind} [P_D(i)]^2} \quad (3)$$

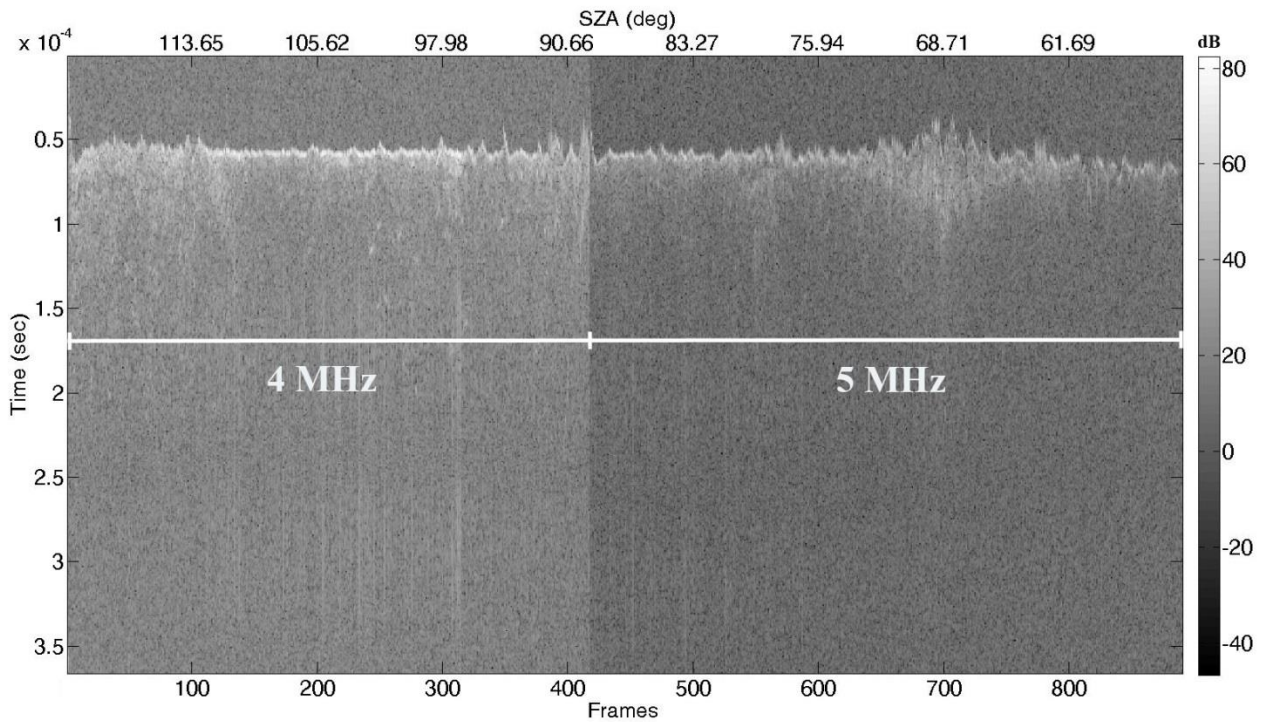
168 Where P_D is the signal power, while ini_ind and $last_ind$ represent the range of samples where the
 169 algorithm is applied.

170 With the exception of the first frame of the orbit, where the spacecraft (S/C) altitude and then the
171 receiving window position is estimated in real time using an eighth-degree polynomial function, for
172 subsequent frames the receiving window opening time is estimated through the tracking loop. In
173 detail, the O.C.O.G. estimates the position of the radar signal after azimuth and range compression,
174 while the tracking loop works to align all echoes around set position inside the receiving window.
175 Due to data volume constraint, signals transmitted to the ground are in the frequency domain and
176 are only compressed in azimuth. In order to complete the signal processing, the MARSIS Ground
177 Segment performs the range compression with a dedicated processor.

178 The effect of the tracking algorithm is visible in the radargram of fig. 1, related to orbit 4646, where
179 echoes are shown after azimuth and on-ground range compression. The brightness variation is due
180 to the frequency switch between 4MHz and 5MHz (for an SZA = 89.29°) and its related to the gain
181 used by the Automatic Gain Control (AGC) of the radar.

182 A radargram is a representation of frames obtained by synthetizing radar pulses acquired continuously
183 during the movement of the spacecraft as a grey-scale image, in which the horizontal dimension is
184 distance along the ground track, the vertical dimension is the round trip time of the echo, and the
185 brightness of the pixel is a function of the strength of the echo. It is easy to see that the tracking
186 loop has completely removed the information related to the topography along the ground track of
187 the radar, which hinders scientific interpretation. For this reason, the opening time of the receiving
188 window is transmitted to the ground, together with the data, in order to allow a reconstruction of the
189 actual signal delay with respect to a fixed altitude above the Martian ellipsoid.

190



191

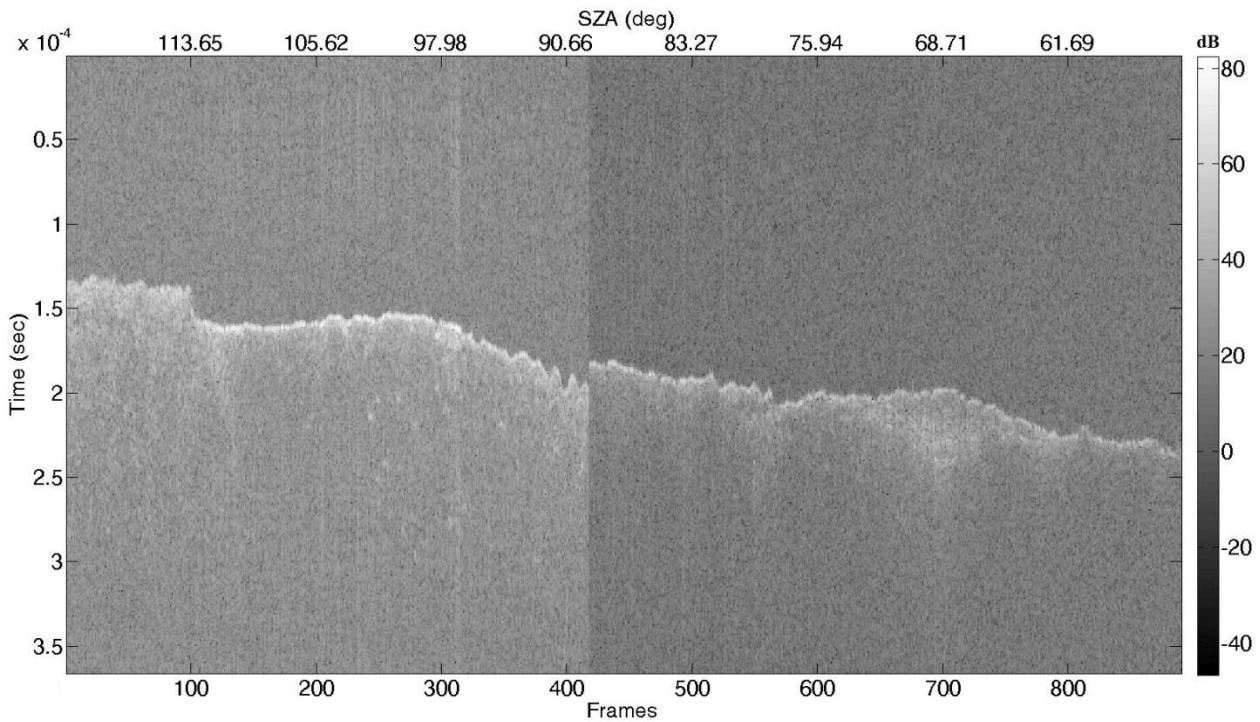
192 Fig. 1. Orbit 4646 radargram. The signal is range compressed with the CM, but the tracking trigger is not removed, so
 193 the surface and subsurface topography information are lost. The different brightness is related to the different gain used
 194 by the Automatic Gain Control (AGC) for each frequency.

195

196 In fig. 2, the tracking trigger has been compensated before the completion of processing through
 197 range compression. Now, surface topography can be discerned, even if the ionosphere delay adds an
 198 unnatural slope to the radargram.

199 As discussed in section 2, the range compression is performed using the Contrast Method.

200



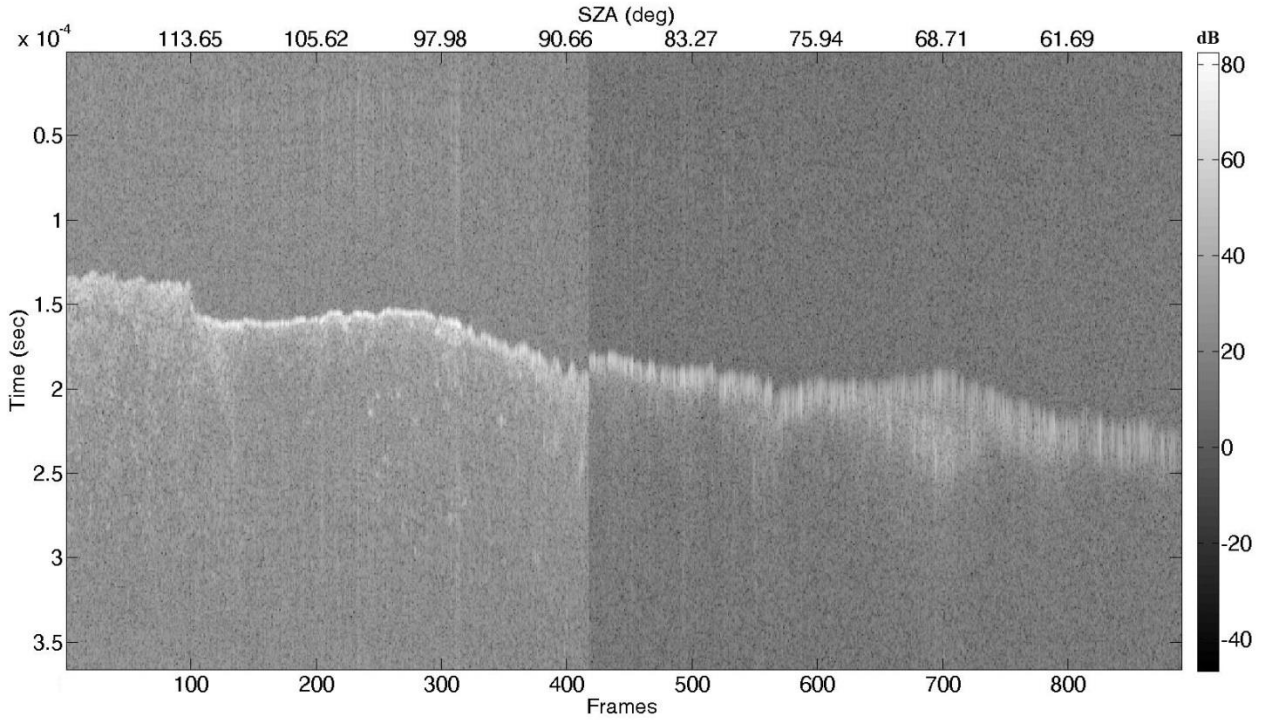
201

202 Fig. 2. Orbit 4646 radargram. The signal is range compressed with the CM and the tracking trigger is removed. The
 203 surface and subsurface topography information, even if affected by the ionosphere delay are recovered.

204

205 The CM consists in iterating the correlation of the radar echoes with the transmitted signal using
 206 different phase compensation terms in order to produce a range compressed signal with the best
 207 energy concentration in a defined time interval of the receiving window.

208 Fig. 3 shows the same radargram of fig. 2 obtained processing the signals without the CM. It is
 209 evident that the use of the CM yields an improvement of all the key radar parameters such as higher
 210 peak power, a better signal to noise ratio and a reduction of the main lobe width. This allows to
 211 have a better range resolution increasing the capability to discriminate surface and subsurface
 212 echoes.



213

214 Fig. 3. Orbit 4646 radargram. The signal is range compressed without the CM and the tracking trigger is not removed.

215 The signals are completely distorted for SZA lower than 90° .

216

217 4. Evaluation of the TEC through the CM and radar echo simulation

218 4.1. A new algorithm for TEC estimation

219 As introduced in section 2, the ionosphere induces a phase shift in a radar signal of frequency f that

220 can be written as:

$$221 \Delta\phi(f) = \frac{4\pi}{c} f \int_0^L [n(z) - 1] dz = \frac{4\pi}{c} f \int_0^L \left[\sqrt{1 - \left(\frac{f_p(z)}{f}\right)^2} - 1 \right] dz \quad (4)$$

222 where L is the ionosphere thickness and c is the speed of light in vacuum.

223 If f_0 is the central frequency of the radar signal band, we can perform a Taylor expansion of the

224 integrand of Eq. (4) and then integrate each term of the expansion, so as to obtain (see eq. 5 and

225 fig.1, Cartacci et al. 2013)

$$226 \Delta\phi(f) \cong a_0 + a_1(f - f_0) + a_2(f - f_0)^2 + a_3(f - f_0)^3 + a_4(f - f_0)^4 + \dots, \quad (5)$$

227 where:

$$228 \quad a_0 = \frac{4\pi}{c} \int_0^L \left(\sqrt{f_0^2 - f_p^2} - f_0 \right) dz \quad [\text{rad}]$$

$$229 \quad a_1 = \frac{4\pi}{c} \int_0^L \left(\frac{f_0}{\sqrt{f_0^2 - f_p^2}} - 1 \right) dz \quad [\text{rad} / \text{Hz}]$$

$$230 \quad a_2 = -\frac{4\pi}{c} \int_0^L \left(\frac{f_p^2}{2(f_0^2 - f_p^2)^{\frac{3}{2}}} \right) dz \quad [\text{rad} / \text{Hz}^2] \quad (6)$$

$$231 \quad a_3 = \frac{4\pi}{c} \int_0^L \left(\frac{f_0 f_p^2}{2(f_0^2 - f_p^2)^{\frac{5}{2}}} \right) dz \quad [\text{rad} / \text{Hz}^3]$$

$$232 \quad a_4 = \frac{4\pi}{c} \int_0^L \left(\frac{4f_0^2 f_p^2 + f_p^4}{8(f_0^2 - f_p^2)^{\frac{7}{2}}} \right) dz \quad [\text{rad} / \text{Hz}^4]$$

233

234 In particular, we focus our attention to the terms a_1 and a_2 .

235 The term a_2 , producing a wide main lobe signal, is responsible for the signal defocusing showed in
 236 fig. 3, while the term a_1 represents the extra delay time introduced by the ionosphere (see fig. 1,

237 Cartacci et al. 2013). The Contrast Method (Cartacci et al. 2013) estimates the quadratic term a_2

238 (\hat{a}_{2CM}) while comparing the received signal with the simulated one, we estimate the term

239 a_1 (\hat{a}_{1SIM}), so we can assume:

$$\hat{a}_{1SIM} = 2\pi\tau \cong a_1 \quad \tau = \text{extra time delay}$$

$$240 \quad \hat{a}_{2CM} \cong a_2 \quad (7)$$

241 Moreover, both terms of eq. (6), after a series expansion, can be expressed as:

$$a_1 = \frac{4\pi}{c} \int \left(\frac{f_0}{(f_0^2 - f_p^2)^{\frac{1}{2}}} - 1 \right) dz \approx \frac{4\pi}{c} \int \left(\frac{1}{2} \frac{f_p^2}{f_0^2} + \frac{3}{8} \frac{f_p^4}{f_0^4} \right) dz =$$

$$= \frac{2\pi}{c f_0^2} (8.98)^2 TEC + \frac{3\pi}{2c f_0^4} (8.98)^4 \int N_e^2(z) dz \quad (8)$$

$$a_2 = -\frac{4\pi}{c} \int \left(\frac{f_p^2}{2(f_0^2 - f_p^2)^{\frac{3}{2}}} \right) dz \approx -\frac{2\pi}{c} \int \left(\frac{f_p^2}{f_0^3} \left(1 + \frac{3f_p^2}{2f_0^2} \right) \right) dz =$$

$$= -\frac{2\pi}{c f_0^3} (8.98)^2 TEC - \frac{3\pi}{c f_0^5} (8.98)^4 \int N_e^2(z) dz \quad (9)$$

242 In a previous work (Cartacci et al. 2013), TEC was obtained by neglecting the
 243 $-\frac{3\pi}{c f_0^5} (8.98)^4 \int N_e^2(z) dz$ term from eq. 9.

244 This approximation is not suitable for application to observations acquired on the day side, because
 245 it yields an overestimation of the TEC.

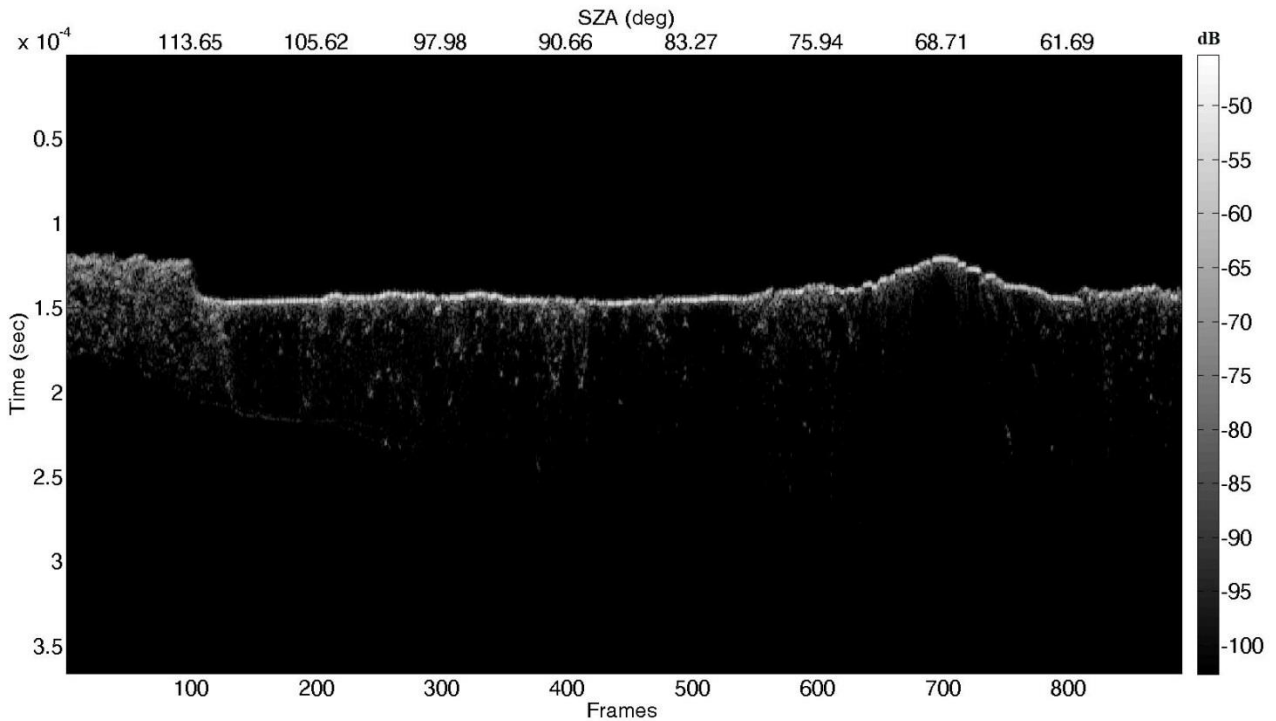
246 Indeed, during the night side, considering $f_p=1$ MHz and $f_0=4$ MHz, the overestimation is lower
 247 than 10% (Cartacci et al. 2013), while during the day side for $f_p=2$ MHz and $f_0=5$ MHz can be
 248 higher than 20%.

249 In order to solve this issue, in this work we use simulations of MARSIS surface echoes that allow to
 250 introduce eq. 8 and consider both terms of eq. 9 without further approximation. Simulations of
 251 surface echoes have been originally devised for the validation of subsurface interface detections,
 252 which is complicated by the so called "clutter", that is by echoes coming from off-nadir surface
 253 features, such as craters or mountains, and reaching the radar after the nadir surface echo. As a
 254 clutter can mask, or be mistaken for, subsurface echoes, numerical electromagnetic models of
 255 surface scattering (see e.g. Nouvel et al., 2004; Russo et al., 2008; Spagnuolo et al., 2011) have
 256 been used to produce simulations of surface echoes, which are then compared to the ones detected
 257 by the radar: any secondary echo visible in radargrams but not in simulations is interpreted as
 258 caused by subsurface reflectors. The code used in the present work was developed based on the
 259 algorithm of Nouvel et al. (2004). The MOLA topographic dataset (Smith et al., 2001) was used to
 260 represent the Martian surface as a collection of flat plates called facets. Radar echoes were then
 261 computed as the coherent sum of reflections from all facets illuminated by the radar. The

262 computational burden of simulations was well above the capabilities of PC's, and required the use
 263 of a supercomputer. In the present work, simulations were used to estimate the expected time of
 264 arrival of surface echoes: from the comparison between the real data and the simulated one (fig. 4)
 265 we can estimate the ionosphere delay that is related to the a_1 term through Eq. (7).
 266 In this way it is possible to solve Eqs. (8) and (9) obtaining

$$TEC = \frac{(2\hat{a}_{1SIM} + \hat{a}_{2CM}f_0)c f_0^2}{2\pi(8.98)^2} \quad (10)$$

267



268

269 Fig. 4. Orbit 4646 simulated radargram.

270

271 The delay estimation is very accurate, because the software used the same settings of the radar. In
 272 particular, the sampling frequency $f_s=1.4\text{MHz}$, is exactly the same that it is implemented in the on-
 273 board software.

274 The only possible source of uncertainty is related to the Spice Kernels used by the signal simulator
 275 to reconstruct the Spacecraft altitude. However, in this case, the estimated error, that is typically

276 around 20m and always lower than 100m (0.3 μ s) (Rosenblatt et al. 2008), can be considered
277 negligible.

278 *4.2 Ionosphere delay evaluation*

279 As discussed in previous sections, the signal received on ground must be processed with the range
280 compression. The first step consists in removing the tracking trigger, that is the time shift
281 introduced by the O.C.O.G. algorithm, from the signal phase in the frequency domain in order to
282 obtain, after the processing, the radargram of fig. 2.

283 This operation is critical, because if not well executed, the position of the signal inside the window
284 is wrong and the extra time delay obtained comparing the real and the simulated signal is
285 compromised.

286 Representing the trigger as a delay Δt_{track} , we have:

$$287 \Delta t_{track} = \Delta t_H + \Delta t_{iono} - \Delta t_{T\epsilon} \quad (11)$$

288 Where:

289 $\Delta t_H =$ *free space travel time due to S/C altitude*

$\Delta t_{iono} =$ *ionospheric delay*

$\Delta t_{T\epsilon} =$ *tracking error*

290 At the same time, the position inside the receiving window of the simulated signal in fig. 4 is
291 determined only by the S/C altitude.

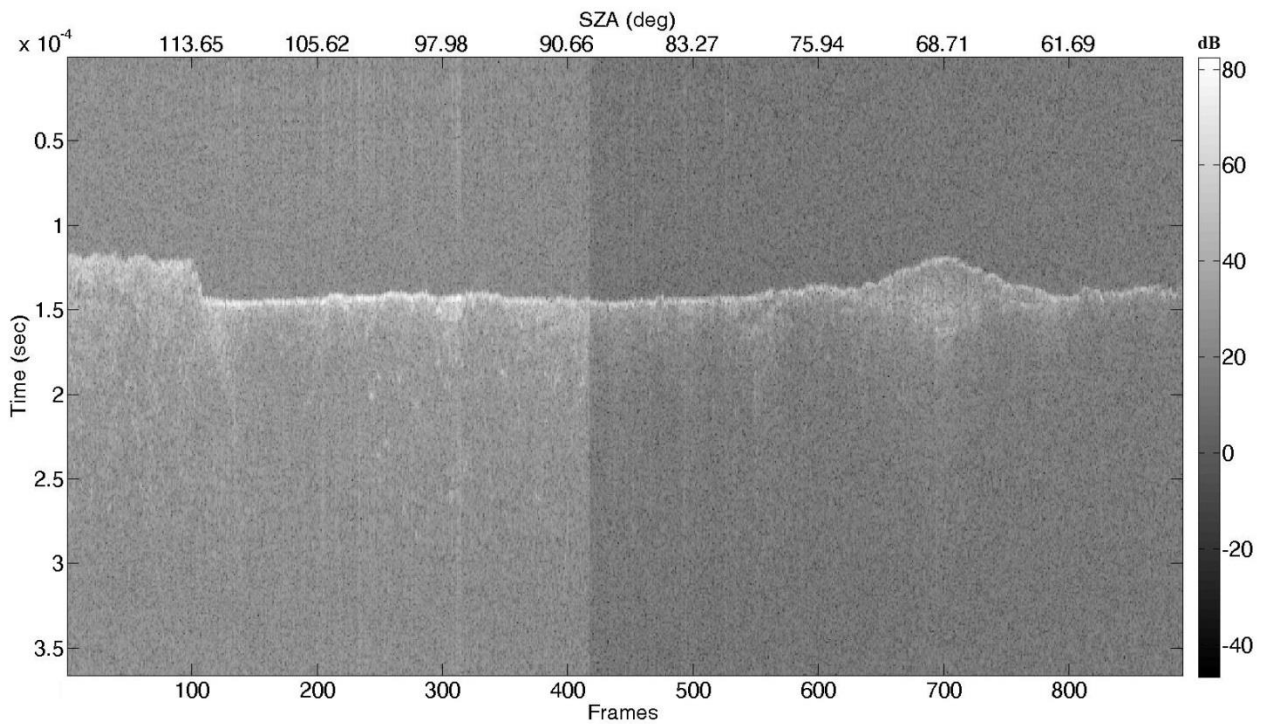
292 Comparing the first frames of the two radargrams of fig. 2-4, where the SZA is high and the
293 ionosphere effect is low, we can notice that there is a small bias.

294 This discrepancy is due to instrumental delays of about 5 μ sec (i.e. 5.31 μ sec for 1.8MHz and
295 4.49 μ sec for 5MHz) that characterize the real signal while are absent in the simulated one. This bias
296 is removed before the TEC estimation.

297 Comparing the delay of the two signals respect to a fixed reference, we have:

$$298 \tau = \Delta t_{iono} - \Delta t_{T\epsilon} \quad (12)$$

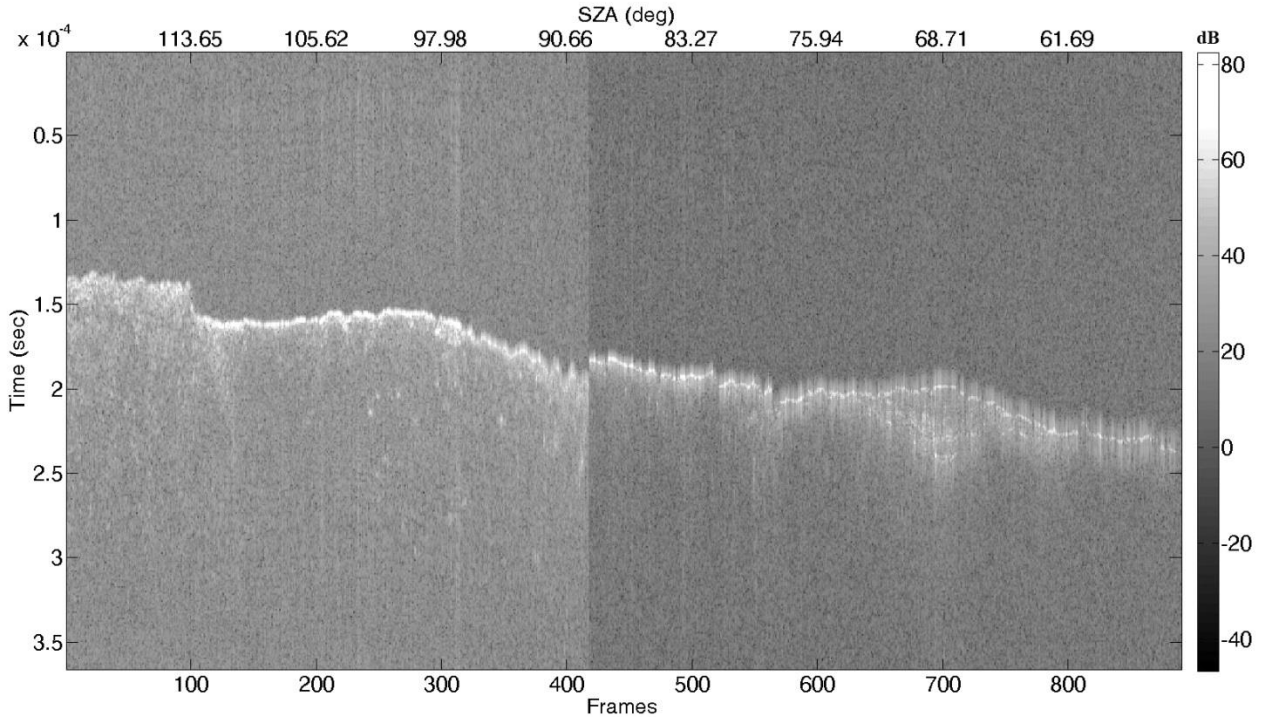
299 A first result of this comparison is the possibility of obtaining a radargram aligned to the Mars
300 topography as showed in fig. 5.



301
302 Fig. 5. Orbit 4646 radargram. The signal is range compressed with the CM, the tracking trigger is removed and the
303 signal is realigned according to the simulation. The surface and subsurface topography information are completely
304 recovered.

305
306 Now, the tracking error $\Delta t_{T\varepsilon}$ is addressed.
307 As said in section 3, the MARSIS on-board processing is capable of both azimuth and range
308 compression. In particular, the range compression is performed with the CM in order to optimize
309 the tracking phase. Unfortunately, during the commissioning phase, in 2005, the MARSIS team,
310 together with the Thales Alenia Space company (the manufacturer of the radar), realized that the
311 CM implemented on-board did not work properly. For this reason, the algorithm was disabled and
312 never used again. In spite of this, the radar has performed well ever since, collecting several
313 thousands of observations during the last eleven years.
314 The absence of the CM in the on-board processing has a direct impact on the tracking loop
315 estimation of the distances involved in data acquisition.

316 Merging fig. 2 and fig. 3 in fig. 6, it is possible to see that the tracking loop, without the CM, works
 317 on a signal that can be much wider than expected in particular during the day side.
 318 In this condition, the O.C.O.G. of Eq. (3) estimates a signal position that is not correct.



319
 320 Fig. 6. Orbit 4646 radargram. The radargrams previously presented in figs. 2-3 are superimposed in order to show the
 321 widening of the signal compressed w/o CM respect to the one processed with the CM.
 322
 323 Since the signal is badly range-compressed, it is much wider than a signal that has been compressed
 324 correctly, and for this reason, the tracking loop identifies the echo position too close to the radar.
 325 In other words, the time delay estimated by the radar is smaller by a factor Δt_{T_E} .
 326 This value can be estimated evaluating also the delay between the simulated signal and the
 327 MARSIS data compressed, on-ground, without the CM.
 328 From the comparison of the two delays it is possible to evaluate Δt_{T_E} and estimate correctly the
 329 extra delay time introduced by the ionosphere.

330
 331

332 *4.3 TEC estimation and validation*

333 Once the terms a_1 and a_2 are obtained from the delay estimation and the CM respectively, it is
334 possible to estimate the TEC along the orbit by using Eq. (10).

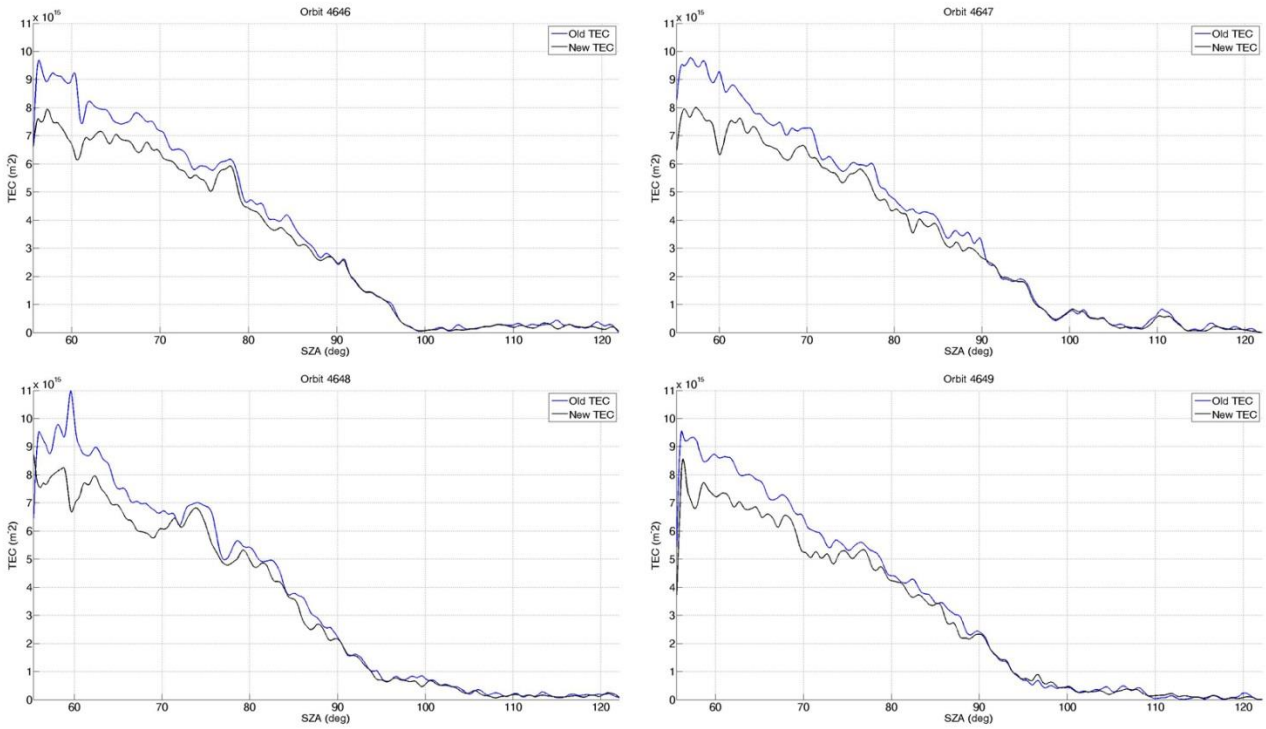
335 We highlight that, as described in the previous sections, the signal processing and, in particular the
336 CM, are always the same. The only difference between the old TEC estimation algorithm and the
337 new one is represented by the use of the ionosphere delay Δt_{TE} to improve the TEC accuracy in the
338 dayside. There is not any variation in the signal processing performances in terms of width of the
339 chirp pulse after compression and SNR.

340 Fig. 7, shows some examples related to consecutive orbits 4646, 4647, 4648 and 4649, where data
341 have been processed with a low pass filter (a zero-phase digital filter that processes the input data in
342 both the forward and reverse directions) to remove random spikes caused by signal oscillations. In
343 detail, these spikes are produced by sudden variations of the SNR mainly due to the surface
344 roughness. When the SNR of a frame is very low, the a_2 value estimated by the CM is not reliable
345 and could vary greatly inside the range described in Appendix of Cartacci et al. 2013.

346 This means that between two consecutives frames, characterized by very different SNR values, the
347 a_2 value, and consequently the TEC, will rise suddenly producing a spike. This is a fake value and is
348 not considered in statistical analysis while for the figures production is filtered.

349

350



351

352 Fig. 7. TEC comparison for orbits 4646-4647-4648-4649. The blue line shows the old TEC while the black line shows
 353 the TEC estimated with the new algorithm.

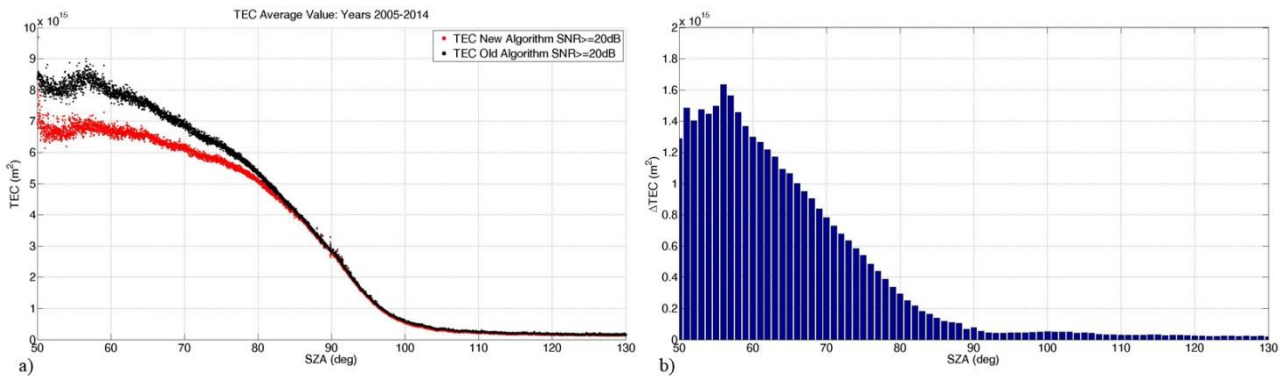
354

355 The blue line represents TEC values estimated using the algorithm described in Cartacci et al.
 356 (2013), the black line represents TEC estimated using the algorithm described in this work, which is
 357 optimized for performance on the day side.

358 The comparison between results of the two methods confirms that for SZA smaller than 90° , the
 359 new one appears not affected by the overestimation that characterized the older one, while for SZA
 360 higher than 90° , the behavior of the two methods is very similar with only local variations that will
 361 be following discussed.

362 In order to test the new algorithm respect to the older one, we consider more than 6800 Mars
 363 Express orbits from July 2005 up to October 2014. TEC estimates were calculated and averaged in
 364 0.01° SZA bins considering only the higher frequency used for each sample and the frames with a
 365 $\text{SNR} \geq 20\text{dB}$. This means that during the night side the TEC is estimated starting from the signals at
 366 4 MHz, while during the day side it is estimated using the data at 5 MHz.

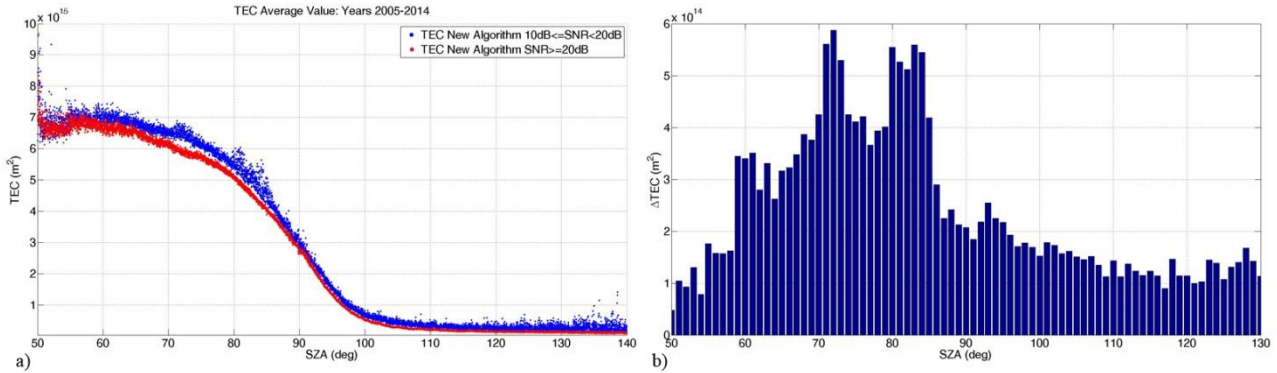
367 Fig. 8 displays such averages of TEC and the difference between both estimates as a function of
 368 SZA, and clearly shows that during the night side, the difference between the two algorithms, if
 369 present, is barely visible while on the day side the difference can reach the value of $\sim 20\%$ being
 370 clear that the new algorithm greatly improves the TEC estimation, mainly for $SZA < 80$, removing
 371 the overestimation that affected the old one.



372
 373 Fig. 8. TEC, averaged over 0.01° SZA bins, plotted as a function of SZA, considering signals with a $SNR \geq 20$ dB (a).
 374 Averaged difference, between new TEC and old TEC, over 1° SZA bins as a function of SZA, considering signals with
 375 a $SNR \geq 20$ dB (b)

376
 377 For lower SZA, the transmitted frequency approaches the maximum local plasma frequency, and
 378 the TEC suffers from a loss of accuracy, because the quadratic term estimated through the CM is
 379 not sufficient to fully compensate the distortion caused by the ionosphere. As a result, the scatter of
 380 TEC values above or below the average trend increases and heavy fluctuations appear for $SZA < 60^\circ$.
 381 It is worth noting that the study of the TEC is influenced by the signal quality and by the SNR,
 382 which is a key parameter in order to quantify the radar performances. In some circumstances, Mars
 383 surface characteristics together with ionosphere attenuation and magnetic fields effects, can greatly
 384 reduce the radar performances. When the SNR is low, the signal processing, the CM algorithm and
 385 the ionosphere delay estimation performances are not optimal and consequently the TEC is affected
 386 by a loss of accuracy.

387 We wish to underline that MARSIS signals can achieve SNRs of the order of 40 dB or higher when
 388 used in flat areas during the night side. For this reason, we used a threshold of 20 dB (for lower
 389 values it is very harshly to identify subsurface layers and the signal shape is very poor) in the
 390 analysis reported in fig. 8 to select the signals suitable for the TEC estimation.



391 a) Fig. 9 TEC from the new algorithm averaged over 0.01° SZA bins, plotted as a function of SZA, considering signals
 392 with a $\text{SNR} \geq 20\text{dB}$ (red points) and the ones evaluated for $10\text{dB} \leq \text{SNR} < 20\text{dB}$ (blue points) (a). Averaged difference,
 393 over 1° SZA bins as a function of SZA (b).
 394

395
 396 Fig. 9a shows the comparison between the average TEC evaluated for $\text{SNR} \geq 20\text{dB}$ (red points) and
 397 the one evaluated for $10\text{dB} \leq \text{SNR} < 20\text{dB}$ (blue points). The difference between both estimates has
 398 been plotted in form of histograms of each SZA bin range (Fig.9b). The TEC estimated starting
 399 from signal with lower SNR is more scattered and higher values are found respect to the one
 400 obtained from signals with a better SNR. The difference between both estimates is more notable
 401 during the dayside from $\text{SZA} < 85^\circ$, where it can be up to 5 times larger than during the nightside
 402 (Fig.9b).

403 The choice to utilize only signals with $\text{SNR} \geq 20\text{dB}$ reduces the amount of frames available to
 404 estimate the TEC. In particular, the percentage of available frames varies from 97.84%
 405 ($\text{SNR} \geq 10\text{dB}$) to 81.6% ($\text{SNR} \geq 20\text{dB}$) during the night side ($\text{SZA} > 90^\circ$), while, during the day side
 406 ($\text{SZA} \leq 90^\circ$), the percentage falls from 89.01% ($\text{SNR} \geq 10\text{dB}$) to 50.9% ($\text{SNR} \geq 20\text{dB}$).

407 This is a conservative decision but, as reported in fig. 9, the signals with a low SNR have a negative
408 impact on the TEC estimation, and are not reliable.

409 In order to validate the new algorithm, we also compared our results with TEC estimates produced
410 using the Mougnot et al. (2008) algorithm, the TEC obtained from MARSIS-AIS data (Gurnett et
411 al. 2008) and the TEC values from the NeMars Model (Sanchez-Cano et al., 2013 and 2016).

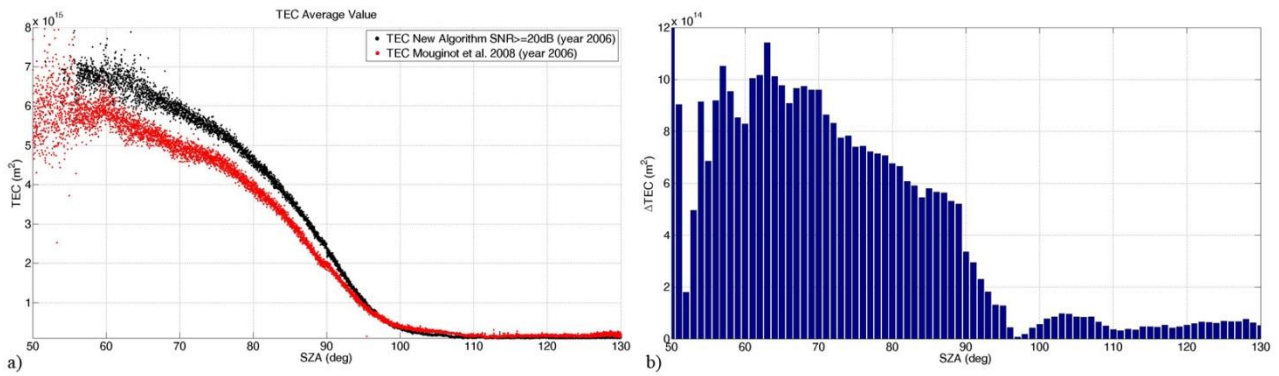
412 The comparison is focused mainly to the day side, because it is for SZA lower than 90° that the new
413 algorithm is expected to improve the TEC estimation.

414 As a first step, we compared the average TEC estimated of the new algorithm with the TEC
415 obtained from the Mougnot et al. (2008) algorithm for the year 2006 (these data are available at the
416 European Space Agency (ESA) Planetary Science Archive (PSA) node). A similar comparison was
417 done in Sanchez-Cano et al., 2015 but only with 19 orbits with different conditions, such as year,
418 solar activity, heliocentric distance and season. In order to validate the algorithm presented in this
419 paper, this study makes a larger statistical comparison by using all the available Mars Express orbits
420 during 2006.

421 Fig. 10a shows that the agreement between the two methods is very good for $SZA \geq 110^\circ$ as
422 previously stated in Sanchez-Cano et al., 2015, while it starts to fail when the ionosphere activity
423 beings to rise and for $SZA \leq 95^\circ$ the two methods diverge steadily as also shown in the histograms of
424 Figure 10b.

425 As mentioned before, this disagreement is probably dependent on the detected issue in the CM
426 algorithm implemented on-board Mars Express, because it is not considered by Mougnot et al.
427 (2008) (see eq. 10) when the constraints for the time delay estimation are defined (i.e. the only
428 constraint considered is the Spacecraft altitude).

429



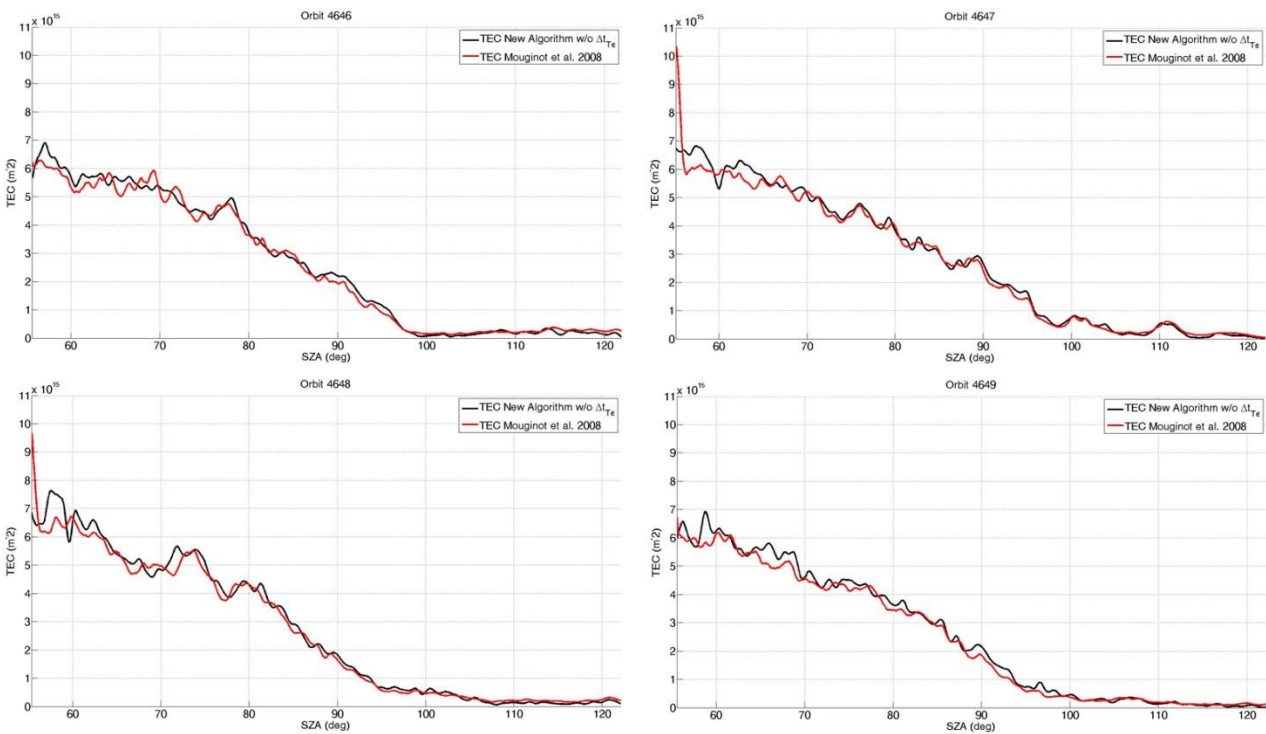
430

431 Fig. 10 TEC, averaged over 0.01° SZA bins and plotted as a function of SZA, comparison between new algorithm
 432 (black dots) and Mougintot et al. 2008 algorithm (red dots) (a). Averaged difference, over 1° SZA bins as a function of
 433 SZA (b).

434

435 In order to test our hypothesis, we removed from the TEC estimation pipeline the term Δt_{TE} .

436 Fig. 11 shows the results for the orbits 4646, 4647, 4648 and 4649, and it is clear that the agreement
 437 between our algorithm (black line), without the aforementioned term, and the Mougintot et al. 2008
 438 algorithm (red line) is now excellent.



439

440 Fig. 11. TEC comparison for orbits 4646-4647-4648-4649. The black line shows the new TEC estimated without the
 441 term Δt_{TE} , while the black line shows the TEC estimated with the Mougintot et al. 2008 algorithm.

442

443 The next step was to compare both algorithms with the TEC obtained independently from the
444 topside electron density profiles of MARSIS-AIS. These profiles were retrieved following the
445 procedure explained in Sanchez-Cano et al., 2012 and Morgan et al., 2013.

446 At this point, we wish to underline that the MARSIS-AIS TEC, deriving from the topside profile of
447 the ionosphere, must be lower than the actual TEC related to the entire depth of the ionosphere and
448 any TEC estimation started from subsurface data, must be higher than the MARSIS-AIS TEC,
449 whatever the algorithm is used.

450 In other words, from a physical point of view, the MARSIS-AIS TEC represents the lower limit of
451 the total TEC estimation (Sanchez-Cano et al. 2015).

452 For this comparison we focused our attention in the range $75^\circ \leq \text{SZA} \leq 90^\circ$ for the following reasons:

- 453 • it's the SZA sector most sampled by all the techniques;
- 454 • it's the part of the dayside that MARSIS in subsurface mode works better because the carrier
455 frequency at lower SZA is very close to the maximum ionospheric frequency and therefore,
456 there is a limit there;
- 457 • it's the SZA sector where TEC shows less variation with solar cycle (e.g. Sanchez-Cano et
458 al., 2016), and therefore, easier to compare.

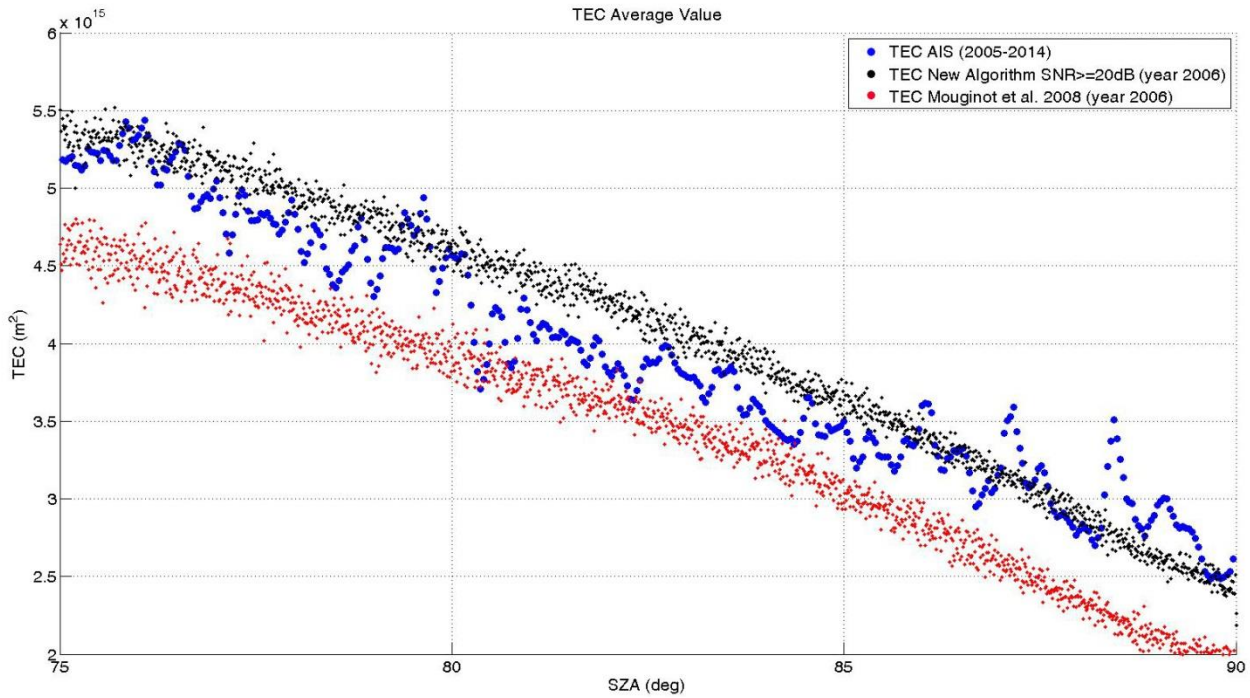
459 The AIS TEC data set used in this study is smaller than both MARSIS SS techniques, as it is only
460 composed by 7322 ionograms related to 226 orbits distributed in almost nine years of activity.

461 Considering that 3580 ionograms (around 50%) were unsuitable, being collected for $\text{SZA} \leq 60^\circ$, the
462 range $75^\circ \leq \text{SZA} \leq 90^\circ$ contains 3231 ionograms, which is still sufficient to have a reliable average.

463 Since the AIS-TEC data set available is smaller than the other two, it was averaged in 0.04° SZA
464 bins.

465 In fig. 12, it is visible that the TEC of this study, estimated with the new algorithm and related to
466 the year 2006 (black dots), is positioned in the upper part of the AIS-TEC distribution, showing

467 higher values for great part of the interval, while the TEC estimated by Mouginit et al. (2008) (red
 468 dots) is mostly on the lower part. This means that the TEC of this study satisfies better the physical
 469 constraint represented by the AIS-TEC, while the TEC from Mouginit et al. (2008) is probably
 470 underestimated because it is lower than the topside TEC obtained from AIS data and that is a
 471 contradiction (Sanchez-Cano et al., 2015). We note that for SZA between 86° and 90° , both
 472 subsurface algorithm gives negatives values when compared to AIS dataset, being always our
 473 estimates the closest to AIS. This can be a consequence of the terminator region, where the
 474 secondary layer of the ionosphere tends to disappear and therefore, AIS and subsurface techniques
 475 should give similar results because both are sampling only the main ionospheric layer.



476
 477 Fig. 12. comparison between the TEC estimated with the Mouginit algorithm (red points), our proposed algorithm
 478 (black dots) and AIS-TEC (blue dots) plotted as a function of SZA. While the TEC values derived from SS data are
 479 averaged over 0.01° SZA bins, the AIS-TEC is averaged over 0.04° SZA bins.

480

481 Finally, we test our method with the NeMars model.

482 NeMars is a semi-empirical model of the dayside ionosphere of Mars that calculates the electron
483 density profile of its two main ionospheric layers for steady conditions (Sanchez-Cano et al., 2013).
484 Both layers are based on the Chapman formulation (Chapman, 1931), being both of the type alpha-
485 Chapman (where the ions are mainly lost by recombination processes). The topside of the main
486 layer (with peak at ~135 km on average) is empirically based on MARSIS AIS data and the
487 bottomside is reconstructed with the Chapman theory. The secondary layer (layer with peak ~110
488 km on average and smaller than the main one), is empirically based on Radio Occultation data from
489 the Mars Global Surveyor mission. The peak density of both layers depends on the SZA, Mars
490 heliocentric distance and solar activity via the proxy F10.7, while the peak altitude only depends on
491 the SZA. Regarding the shape of the main layer, the neutral scale height depends on both the SZA
492 and on the height of the profile in relation to the peak altitude. However, the secondary layer neutral
493 scale height is considered constant at 12 km. Finally, TEC is obtained after the integration of the
494 electron density of both layers with altitude.

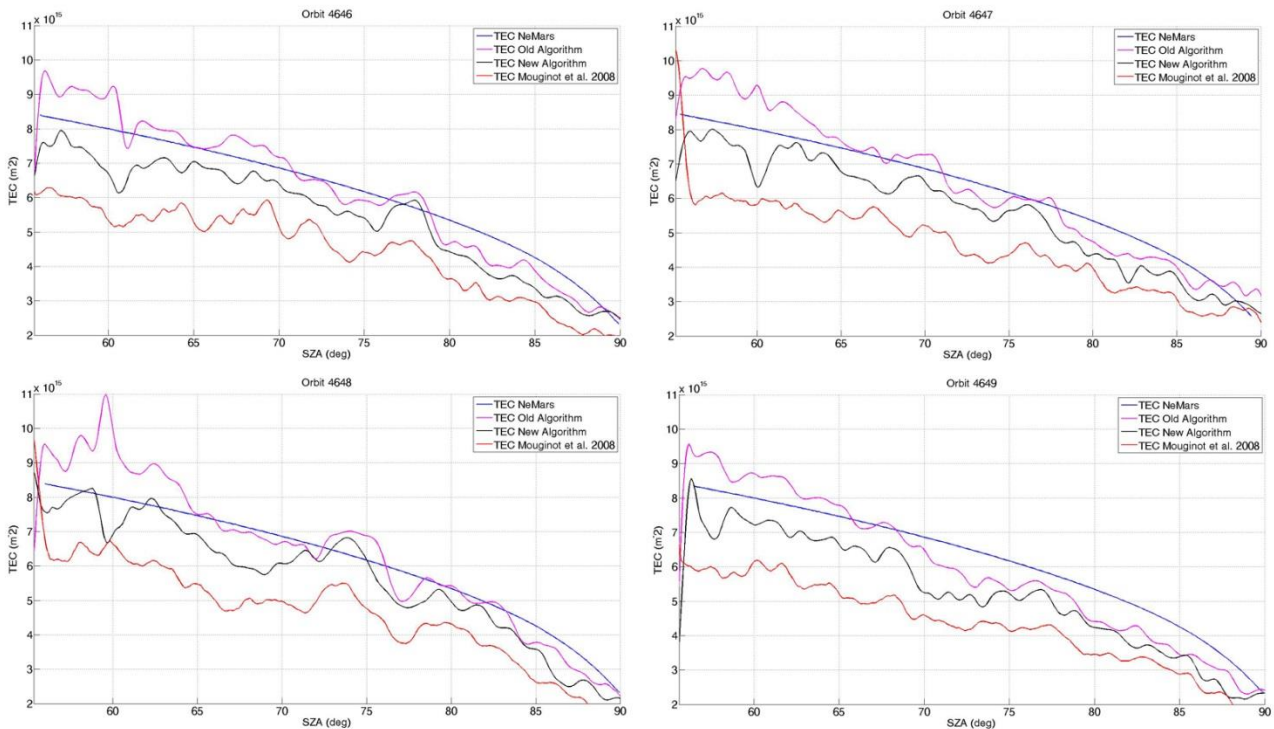
495 The model gives the major part of the ionization of the Martian ionosphere. Therefore, TEC from
496 NeMars can be directly compared to the MARSIS subsurface TEC estimates, and should be higher
497 than MARSIS AIS data that only gives information of the topside ionosphere.

498 Recently, the model equations (i.e. ionospheric scale height) for the topside of the main layer have
499 been improved after considering the topside behavior with the solar cycle phases. In this work, the
500 new topside scale height for low solar activity (Sanchez-Cano et al., 2016) has been implemented in
501 the original model described by Sanchez-Cano et al., 2013.

502 Fig. 13 confirms that the new TEC estimates (black line) are always higher than the TEC from
503 Mougnot et al. (2008) (red line). Moreover, the new TEC is significantly closer to the NeMars
504 model (blue line). Considering that we are comparing a model of steady ionospheric conditions with
505 respect to real data that could be influenced by many factors not considered in the model (e.g. solar
506 wind variability, induced magnetic field, crustal magnetic fields, gravitational tides, atmospheric
507 phenomena, electric fields, changes in ionospheric conductivities, surface roughness, topography

508 changes, etc), the amplitude and the average shape of our TEC is in very good agreement with
509 NeMars model.

510 On the contrary, the old TEC (magenta line) matches worse respect to the NeMars model, because,
511 even if it is closer in terms of amplitude, its behavior has a different slope. This is further evaluated
512 in the following lines with a deep analysis of the ionospheric distortion between both TEC
513 estimations and the NeMars model.



514
515 Fig. 13. TEC comparison for orbits 4646-4647-4648-4649. The blue line shows the NeMars TEC, the magenta line
516 shows the old TEC, the black line shows the TEC estimated with the new algorithm while the red line shows the one
517 from Mougnot et al. (2008).

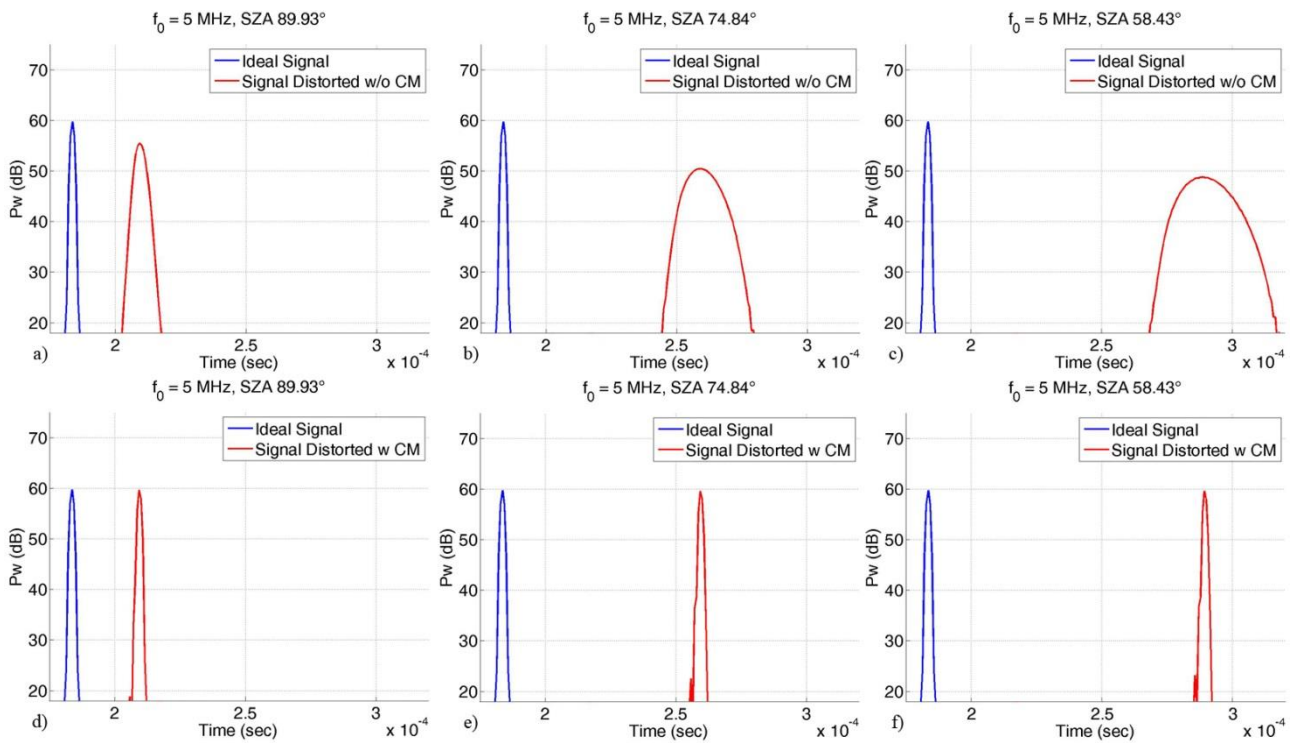
518
519 Finally, as mentioned before, we perform a test using a simulator of ionospheric distortion to
520 validate our results to which we apply to the new developed algorithm to evaluate the TEC. This is
521 a kind of inverse process in which TEC from the NeMars model has been reconstructed in the same
522 way that the MARSIS subsurface TEC is retrieved (see section 4). In details, we compute a phase

523 distortion using the NeMars Model, as defined by eq. 4, for an entire orbit according to the SZA at
524 the time of observation, and also the associated TEC.

525 Our goal is to verify the accuracy of the new algorithm, comparing the TEC estimated by the
526 simulator with the one directly obtained through the NeMars Model.

527 The distortion, simulating the effects of the Mars ionosphere is applied to the phase of an ideal
528 signal with the characteristics (in terms of frequency, band and sample frequency) of the actual
529 signal transmitted by MARSIS.

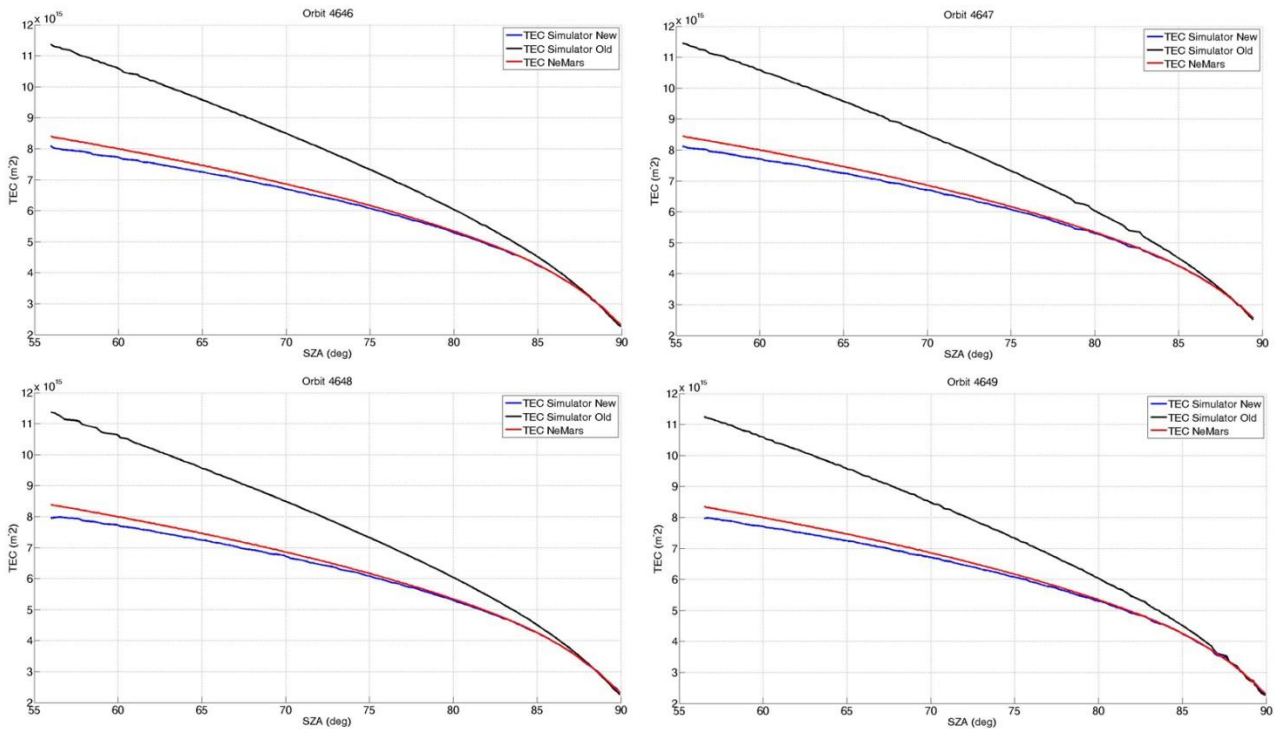
530 In Fig. 14, the comparison between the ideal signal (blue line) and the signal affected by ionosphere
531 distortion (red line) is shown for three different SZA related to the orbit 4646. While in the upper
532 panels (fig. 14a, b, c) the signal with the distortion is compressed without any compensation, in the
533 lower panels (Fig. 14d, e, f) the signal is processed using the CM.



534
535 Fig. 14. Comparison between the ideal and the distorted signal for orbit 4646. Both signal are range compressed. The
536 effects of the distortion, as the delay and a wide main lobe, are clearly visible.

537

538 The effects of the ionosphere are clearly visible in the form of a wide main lobe and a delay (fig.
 539 14a, b, c) that get worse for lower values of the SZA (when the S/C is deeper in the dayside).
 540 The CM removes the quadratic term (Fig. 14d, e, f), estimating the term a_2 , while the delay can be
 541 easily calculated comparing the signals position.
 542 Therefore, all the information necessary for the TEC estimation are available and in fig. 15 the
 543 results for the orbits 4646-4647-4648-4649 are shown.

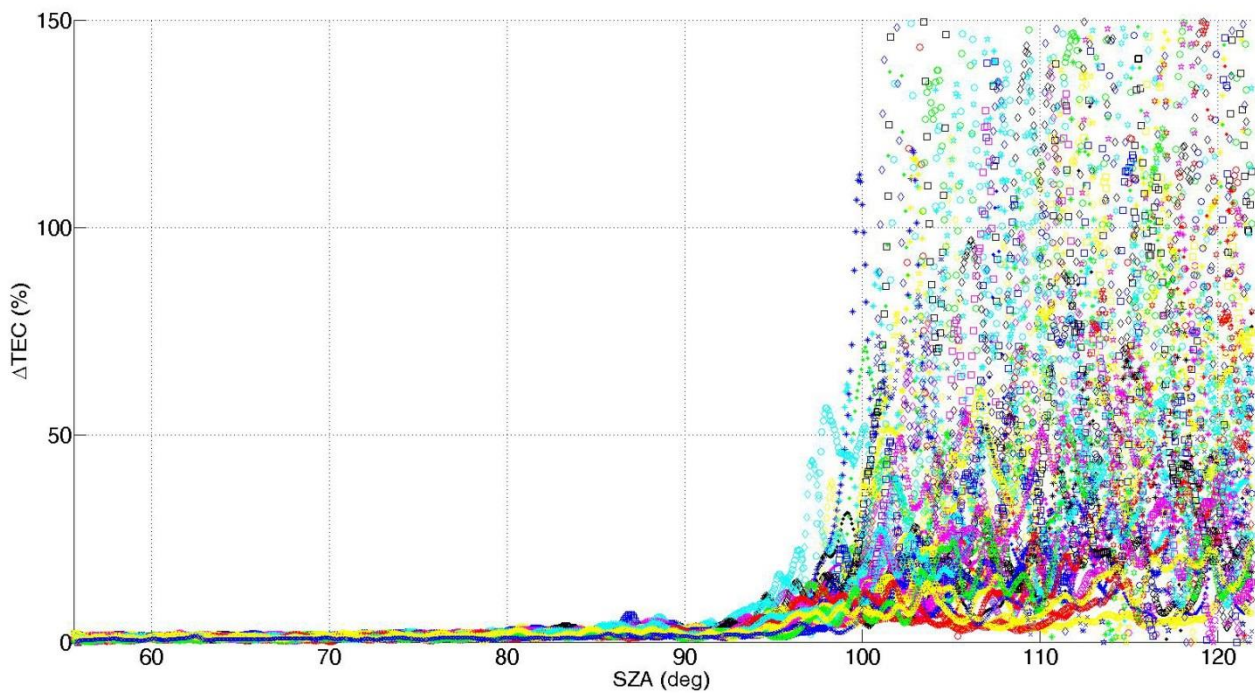


544
 545 Fig. 15. Comparison between the TEC estimated through the simulator and the TEC derived from the NeMars Model.

546
 547 The good performance of the new algorithm is demonstrated, as the difference between the TEC
 548 estimated by the simulator and the one calculated from the NeMars Model is always under 5%,
 549 even for very low values of the SZA. The increasing gap between both TEC estimates is mainly due
 550 to the fact that for lower SZA, the related plasma frequency begins to be too close to the carrier
 551 signal frequency and the CM cannot compensate correctly the distortion.
 552 The test also confirms that the older algorithm overestimates the TEC for this range of SZA, and
 553 that the new algorithm is an improved version for the TEC dayside.

554 However, the main source of error of the new method is related to the accuracy of the estimation of
555 the ionosphere delay that can be influenced by to the presence of the surface clutter, i.e. lateral
556 echoes produced by surface topography.

557 The surface clutter can introduce an error in the delay estimation influencing the correct functioning
558 of O.C.O.G. in the tracking loop. We can quantify this error in the order of few microseconds, in
559 worst conditions. To evaluate the impact on the TEC estimation, that can vary considerably with the
560 SZA values, a simulated random error of maximum 5 μsec (750 m in the free space) is added to the
561 estimated delay on a sample of 50 orbits (between orbit 4646 and orbit 4719), selected with a
562 similar range of SZA; the results are shown in fig. 16.

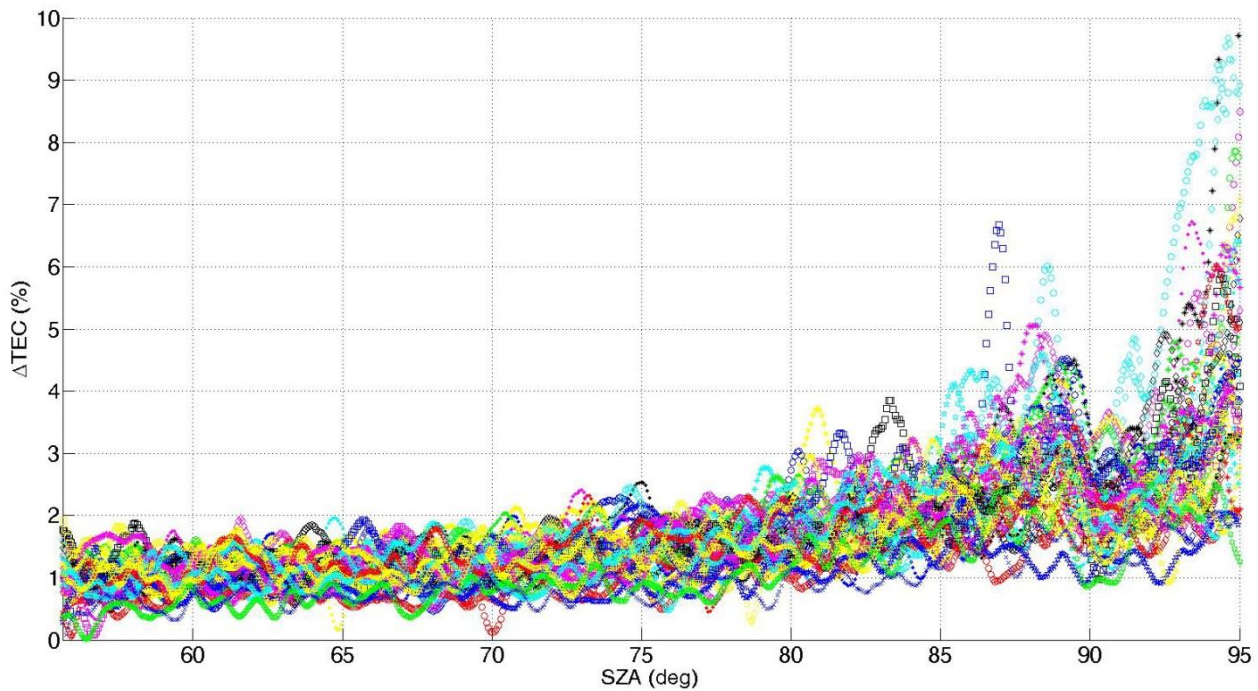


563
564 Fig. 16. TEC percentage variation for a set of 50 orbits considering a random error, in the delay estimation, with a
565 maximum value of 5 μsec .

566
567 During the night side, for an SZA higher than 95° , considering the low values of the TEC involved,
568 even a small error in the delay evaluation can lead to a large overestimation, while for an SZA

569 lower than 95° , the error in the TEC estimation is always under 10%, and often much smaller (fig.
570 17), so that it can be considered negligible.

571 We wish to underline that, normally, if the clutter is so heavy to introduce an error of about 10% in
572 the time delay estimation, also the SNR is reduced. Actually, the major part of the frames where the
573 surface features produce a relevant error in the delay estimation have a low SNR.



574
575 Fig. 17. TEC percentage variation for a set of 50 orbits considering a random error, in the delay estimation, with a
576 maximum value of $5 \mu\text{sec}$, for $\text{SZA} \leq 95^\circ$.

577
578 Adopting a conservative approach, we decided to use both methods to estimate the TEC.
579 The older one, which works better during the night side and it is independent from the delay, is used
580 for SZA higher than 90° , and the new one is used for $50^\circ \leq \text{SZA} \leq 90^\circ$.

581 It is worth noting that, during the day side MARSIS normally operates in AIS mode for $\text{SZA} \leq 50^\circ$,
582 as that operational model is specially designed for ionospheric sounding and in this SZA range is
583 where the ionosphere is fully formed.

584

585 To conclude this section, we summarize the main findings.

- 586 • The possibility to estimate both the linear and the quadratic terms of the ionosphere
587 distortion allows to develop a more precise algorithm for TEC estimation on the day side.
- 588 • The TEC estimated with the new algorithm is higher than the one estimated from MARSIS-
589 AIS, as expected, and shows a good agreement with the NeMars model.
- 590 • Simulations demonstrate that, on the day side, the new algorithm performs with very good
591 accuracy since the error is always under 5% .
- 592 • The new algorithm is particular well suited for the day side when the possible presence of
593 local error in the delay estimation due to the clutter effect is negligible. The older algorithm,
594 Cartacci et al., 2013, is still valid for the night side because it is not influenced by the clutter
595 effects and the overestimation introduced by the approximation in eq. 8 is under 10%.
- 596 • In the terminator region, the carrier frequency used is 5MHz, this means that the differences
597 between the two methods are relatively small, typically under 10%.

598

599 **5. Discussion and Conclusions**

600 In this paper we have described a new algorithm that makes use of the Contrast Method and of
601 signal echo simulations to estimate the TEC of the Martian ionosphere. We have demonstrated that
602 the new method overcomes the limitation of the previous one (Cartacci et al., 2013) during the day
603 side (see Fig. 7), achieving an improvement of about 20% in accuracy for the lowest SZA that
604 MARSIS can operate.

605 In order to validate the new algorithm, we have compared our results with the TEC obtained
606 through other methods. In particular, we focused our attention to the TEC obtained using the
607 Mougnot et al. 2008 algorithm, the TEC estimated from the MARSIS AIS dataset and the
608 predictions of the NeMars model.

609 We have shown that the new MARSIS TEC values are in good agreement with both AIS-TEC (see
610 Fig. 12) and the NeMars model (see Fig. 13). On the contrary, the agreement with the Mouginit et
611 al. TEC is limited to the deep night side, while when the ionosphere activity starts to increase
612 (lower SZA), the differences become much significant (see Fig. 10).

613 The TEC estimates from Mouginit et al. 2008 results too low even when compared with AIS-TEC
614 (see Fig. 12) which is an in-situ observation (see also Figure 11 at Sánchez-Cano et al., 2013 and
615 statistic validation at Sánchez-Cano et al., 2015), suggesting an underestimation of the TEC values.
616 These lower estimations can be due to the fact of an issue in the CM implemented on-board the
617 spacecraft (see Fig. 11).

618 Moreover, simulations have shown (see Fig. 15) that, starting from modeled distortion, the
619 algorithm is capable to estimate the related TEC with very good accuracy, limiting the error under
620 5% even for SZA close to 55° .

621 The comparison between the old method, using only the CM, and the new one, has shown that the
622 two methods are complementary, performing at their best in different range of the SZA, and thus
623 allowing an optimal estimation of the TEC along the orbits. In particular, the new algorithm
624 performs better for SZA lower than 95° , while the older one is more robust for SZA higher than
625 95° .

626
627 The multi-dataset comparison shown in this paper agree with the previous study of Sanchez-Cano et
628 al., 2015, where a critical assessment of TEC from 19 Mars Express orbits obtained with subsurface
629 algorithms and with AIS was performed. The main conclusion of Sanchez-Cano et al., 2015 was
630 that MARSIS Mouginit et al. 2008 and Cartacci et al., 2013 subsurface data from the nightside and
631 terminator sectors, $SZA > 75^\circ$, could be used with confidence since the differences among all data
632 sets were small. In our study, we have shown that with the new algorithm that improves the
633 Cartacci et al., 2013 method, this is still valid, being the new algorithm more consistent than the
634 other one when compared to AIS and to modelling. The main issue reported by Sanchez-Cano et al.,

635 2015 was the dayside, $SZA < 75^\circ$, where caution with the use of both subsurface algorithms was
636 recommended as the TEC values were notably less accurate. In our study, we have improved these
637 estimates by reducing the TEC uncertainty up to a 20%.

638 We highlight that, in general, MARSIS data below $SZA 55-65^\circ$ (depending on solar cycle phases)
639 should not be used for scientific purposes, simply because the MARSIS carrier frequencies are of
640 the order or lower than the actual maximum ionospheric plasma frequency. For this end, data with a
641 poor SNR is indicated with a flag in both Mougnot et al. 2008, and Cartacci et al. 2013, files.

642

643 The new acquired capability to estimate the TEC with good accuracy during the day side, will allow
644 us to understand and compensate better the attenuation phenomena, such as the ionosphere
645 absorption and the Faraday rotation (Safaeinili et al., 2003), increasing the amount and the quality
646 of MARSIS data available to characterize the surface and the subsurface of Mars.

647 In addition, this new TEC data set will be useful to further understand the behavior and variability
648 of the Mars ionosphere, in particular at the terminator region where there is a non-well understood
649 dawn/dusk asymmetry, and the ionosphere does not follow the Chapman theory because of a non-
650 spherical symmetry between day and night (e.g. Grandin et al., 2014; Ao et al., 2015).

651 **Acknowledgements**

652 The authors gratefully acknowledge support from the Italian Space Agency (ASI) through contract
653 I/032/12/1. The numerical code for the simulation of surface scattering was developed at the
654 Consorzio Interuniversitario per il Calcolo Automatico dell'Italia Nord-Orientale (CINECA) in
655 Bologna, Italy. Simulations were produced thanks to the Partnership for Advanced Computing in
656 Europe (PRACE), awarding us access to the SuperMUC computer at the Leibniz-Rechenzentrum,
657 Garching, Germany. Test simulations were run on the Jacobs University CLAMV HPC cluster, and
658 we are grateful to Achim Gelessus for his support. B.S.-C. acknowledges support through STFC
659 grants ST/N000749/1 and ST/K001000/1. Sandro M. Radicella is acknowledged for useful
660 discussions at an early stage of this work. Operations of the Mars Express spacecraft by the
661 European Space Agency (ESA) are gratefully acknowledged.

662

663 With fond memories of Professor Giovanni Picardi, conceiver of the MARSIS instrument, our
664 leader and friend, who passed away last in August 2015.

665

666

667

668

669

670

671

672

673

674

675

676

677 **References**

- 678 Ao, C. O., C. D. Edwards Jr., D. S. Kahan, X. Pi, S. W. Asmar, and A. J. Mannucci (2015), A first
679 demonstration of Mars crosslink occultation measurements, *Radio Sci.*, 50, 997–1007,
680 *doi:10.1002/2015RS005750*.
- 681
- 682 Budden, K. G., 1985, *The Propagation of Radio Waves*, Cambridge Univ. Press, New York.
- 683
- 684 Cartacci, M.; Amata, E.; Cicchetti, A.; Noschese, R.; Giuppi, S.; Langlais, B.; Frigeri, A.; Orosei,
685 R.; Picardi, G., 2013: Mars ionosphere total electron content analysis from MARSIS subsurface
686 data, *Icarus*
- 687
- 688 Chapman, S. (1931a), Absorption and dissociative or ionizing effects of monochromatic radiation in
689 an atmosphere on a rotating earth. *Proc. Phys. Soc., London* 43, 26-45.
- 690
- 691 Chapman, S. (1931b), Absorption and dissociative or ionizing effect of monochromatic radiation in
692 an atmosphere on a rotating earth part II. Grazing incidence. *Proc. Phys. Soc.*, 764 London 43, 483-
693 501.
- 694
- 695 Grandin, M., P.-L. Blelly, O. Witasse, and A. Marchaudon, (2014), Mars Express radio-occultation
696 data: A novel analysis approach, *J. Geophys. Res. Space Physics*, 119, *doi:10.1002/2014JA020698*.
- 697
- 698 Gurnett, D. A., et al. (2008), An overview of radar soundings of the Martian ionosphere from the
699 Mars Express spacecraft, *Adv. Space Res.*, 41, 1335–1346, *doi:10.1016/j.asr.2007.01.062*.
- 700
- 701 Morgan, D.D., Gurnett, D.A., Kirchner, D.L., Fox, J.L., Nielsen, E., Plaut, J.J., 2008. Variation of

702 the Martian ionospheric electron density from Mars Express radar soundings. *J. Geophys. Res.*
703 (*Space Phys.*) 113, 9303. <http://dx.doi.org/10.1029/2008JA013313>.
704

705 Morgan, D. D., O. Witasse, E. Nielsen, D. A. Gurnett, F. Duru, and D. L. Kirchner (2013), The
706 processing of electron density profiles from the Mars Express MARSIS topside sounder, *Radio Sci.*,
707 48, 197–207, doi:10.1002/rds.20023
708

709 Mougnot J., Kofman, W., Safaeinili, A., and Herique, A. , 2008: Correction of the ionospheric
710 distortion on the MARSIS surface sounding echoes, *Planetary and Space Science*, Vol. 56, pp. 917-
711 926.
712

713 Nouvel, J.-F., Herique, A., Kofman, W., Safaeinili, A. 2004. Radar signal simulation: Surface
714 modeling with the Facet Method. *Radio Science* 39, 1013.
715

716 Picardi, G.Sorge, S., 2000:Adaptive compensation of ionosphere dispersion to improve subsurface
717 detection capabilities in low-frequency radar systems. *Proc. SPIE* Vol. 4084, p. 624-629, Eighth
718 International Conference on Ground Penetrating Radar.
719

720 Picardi G., Plaut J. J., Biccari D., Bombaci O., Calabrese D., Cartacci M., et al. , 2005: Radar
721 Soundings of the Subsurface of Mars, *Science*, Vol. 310, pp. 1925-1928.
722

723 Orosei R., Jordan R.L., Morgan D.D., Cartacci M., Cicchetti A., Duru F., Gurnett D.A., Heggy E.,
724 Kirchner, R.Noschese D.L., Kofman W., Masdea A., Plaut J.J., Seu R., Watters T.R., Picardi G.
725 (2015), Mars Advanced Radar for Subsurface and Ionospheric Sounding (MARSIS) after nine years
726 of operation: A summary.*Planetary and Space Science* 112(2015)98–114. DOI:
727 10.1016/j.pss.2014.07.010

728

729 Rosenblatt P., Lainey V., Le Maistre S., Marty J.C., Dehant V., Patzold M. Van Hoolst T., Hausler
730 B.. Accurate Mars Express orbits to improve the determination of the mass and ephemeris of the
731 Martian moons. *Planetary and Space Science* 56 (2008) 1043–1053

732

733 Russo, F., Cutigni, M., Orosei, R., Taddei, C., Seu, R., Biccari, D., Giacomoni, E., Fuga, O.,
734 Flamini, E. 2008. An incoherent simulator for the SHARAD experiment. Radar Conference, 2008.
735 RADAR '08. IEEE 26-30 May 2008, 1.

736

737 Safaeinili, A., Kofman, W., Nouvel, J. F., Herique, A., Jordan, R. L., 2003: Impact of Mars
738 ionosphere on orbital radar sounder operation and data processing, *Planetary and Space Science*,
739 Volume 51, Issue 7-8, p. 505-515, 2003.

740

741 Safaeinili, A., Kofman, W., Mouginot, J., Gim, Y., Herique, A., Ivanov, A. B., Plaut, J. J., and
742 Picardi, G. , 2007: Estimation of the total electron content of the Martian ionosphere using radar
743 sounder surface echoes, *Geophysical Research Letters*, Vol. 34.

744

745 Sánchez-Cano, B., O. Witasse, M. Herraiz, S. M. Radicella, J. Bauer, P.-L. Blelly, and G.
746 Rodríguez-Caderot (2012), Retrieval of ionospheric profiles from the Mars Express MARSIS
747 experiment data and comparison with radio occultation data, *Geosci. Instrum. Methods Data Syst.*,
748 1, 77–84, doi:10.5194/gi-1-77-2012.

749

750 Sánchez – Cano, B., S. M. Radicella, M. Herraiz, O. Witasse and G. Rodríguez – Caderot (2013),
751 NeMars: An empirical model of the Martian dayside ionosphere based on Mars Express MARSIS
752 data, *Icarus*, 225, 236-247. doi: <http://dx.doi.org/10.1016/j.icarus.2013.03.021>

753

754 Sánchez-Cano B., Morgan D. D., Witasse O., Radicella S. M., Herraiz M., Orosei R., Cartacci M.,
755 Cicchetti A., Noschese R., Kofman W., Grima C., Mouginot J., Gurnett D. A., Lester M., Blelly P.-
756 L., Opgenoorth H., and Quinsac G., (2015), Total electron content in the Martian atmosphere: A
757 critical assessment of the Mars Express MARSIS data sets. *J. Geophys. Res. Space Physics*, 120,
758 doi:10.1002/2014JA020630.

759

760 Sánchez-Cano B., M. Lester, O. Witasse S. E. Milan, B. E. S. Hall, M. Cartacci, K. Peter, D. D.
761 Morgan, P.-L. Blelly, S. Radicella, A. Cicchetti, R. Noschese, R. Orosei, M. Patzold, 2016: Solar
762 cycle variations in the ionosphere of Mars as seen by multiple Mars Express data sets. *J. Geophys.*
763 *Res. Space Physics*, 121, doi:10.1002/2015JA022281.

764

765 Smith, D. E., Zuber, M. T., Frey, H. V., Garvin, J. B., Head, J. W., Muhleman, D. O., Pettengill, G.
766 H., Phillips, R. J., Solomon, S. C., Zwally, H. J., Banerdt, W. B., Duxbury, T. C., Golombek, M. P.,
767 Lemoine, F. G., Neumann, G. A., Rowlands, D. D., Aharonson, O., Ford, P. G., Ivanov, A. B.,
768 Johnson, C. L., McGovern, P. J., Abshire, J. B., Afzal, R. S., and Sun, X.: Mars Orbiter Laser
769 Altimeter: Experiment summary after the first year of global mapping of Mars, *Journal of*
770 *Geophysical Research*, 106, 23,689-23,722, doi:10.1029/2000JE001364, 2001.

771

772 Spagnuolo, M. G., Grings, F., Perna, P., Franco, M., Karszenbaum, H., and Ramos, V. A.:
773 Multilayer simulations for accurate geological interpretations of SHARAD radargrams, *Planetary*
774 *and Space Science*, 59, 1222-1230, doi:10.1016/j.pss.2010.10.013, 2011.

775

776 D. J. Wingham, C. G. Rapley and H. Griffiths, "New technique in satellite altimeter tracking systems,"

777 IGARSS, vol. 1, pp. 185-190, 1986.

778

779

780

781

782

783

784

785

786

787

788

789

790

791

792

793

794

795

796

797

798

799

800

801

802

803

804

805 **Figure captions**

806 Fig. 1. Orbit 4646 radargram. The signal is range compressed with the CM, but the tracking trigger
807 is not removed, so the surface and subsurface topography information are lost. The different
808 brightness is related to the different gain used for the two frequencies.

809 Fig. 2. Orbit 4646 radargram. The signal is range compressed with the CM and the tracking trigger
810 is removed. The surface and subsurface topography information, even if affected by the ionosphere
811 delay are recovered.

812 Fig. 3. Orbit 4646 radargram. The signal is range compressed without the CM and the tracking
813 trigger is not removed. The signals are completely distorted for SZA lower than 90° .

814 Fig. 4. Orbit 4646 simulated radargram.

815 Fig. 5. Orbit 4646 radargram. The signal is range compressed with the CM, the tracking trigger is
816 removed and the signal is realigned according to the simulation. The surface and subsurface
817 topography information are completely recovered.

818 Fig. 6. Orbit 4646 radargram. The radargrams previously presented in figs. 2-3 are superimposed in
819 order to show the widening of the signal compressed w/o CM respect to the one processed with the
820 CM.

821 Fig. 7. TEC comparison for orbits 4646-4647-4648-4649. The blue line shows the old TEC while
822 the black line shows the TEC estimated with the new algorithm.

823 Fig. 8. TEC, averaged over 0.01° SZA bins, plotted as a function of SZA, considering signals with a
824 $\text{SNR} \geq 20\text{dB}$ (a). Averaged difference, between new TEC and old TEC, over 1° SZA bins as a
825 function of SZA, considering signals with a $\text{SNR} \geq 20\text{dB}$ (b)

826 Fig. 9. TEC from the new algorithm averaged over 0.01° SZA bins, plotted as a function of SZA,
827 considering signals with a $\text{SNR} \geq 20\text{dB}$ (red points) and the ones evaluated for $10\text{dB} \leq \text{SNR} < 20\text{dB}$
828 (blue points) (a). Averaged difference, over 1° SZA bins as a function of SZA (b).

829 Fig. 10. TEC, averaged over 0.01° SZA bins and plotted as a function of SZA, comparison between
830 new algorithm (black dots) and Mougnot et al. 2008 algorithm (red dots) (a). Averaged difference,
831 over 1° SZA bins as a function of SZA (b).

832 Fig. 11. TEC comparison for orbits 4646-4647-4648-4649. The black line shows the new TEC
833 estimated without the term Δt_{TE} , while the black line shows the TEC estimated with the Mougnot
834 et al. 2008 algorithm.

835 Fig. 12. comparison between the TEC estimated with the Mougnot algorithm (red points), our
836 proposed algorithm (black dots) and AIS-TEC (blue dots) plotted as a function of SZA. While the
837 TEC values derived from SS data are averaged over 0.01° SZA bins, the AIS-TEC is averaged over
838 0.04° SZA bins.

839 Fig. 13. TEC comparison for orbits 4646-4647-4648-4649. The blue line shows the NeMars TEC,
840 the magenta line shows the old TEC, the black line shows the TEC estimated with the new
841 algorithm while the red line shows the one from Mougnot et al. (2008).

842 Fig. 14. Comparison between the ideal and the distorted signal for orbit 4646. Both signal are range
843 compressed. The effects of the distortion, as the delay and a wide main lobe, are clearly visible.

844 Fig. 15. Comparison between the TEC estimated through the simulator and the TEC derived from
845 the NeMars Model.

846 Fig. 16. TEC percentage variation for a set of 50 orbits considering a random error, in the delay
847 estimation, with a maximum value of $5 \mu\text{sec}$.

848 Fig. 17. TEC percentage variation for a set of 50 orbits considering a random error, in the delay
849 estimation, with a maximum value of $5 \mu\text{sec}$, for $\text{SZA} \leq 95^\circ$.

850

851

852